Cloud Radiative Effects and Precipitation in Extratropical Cyclones

JAMES B. POLLY AND WILLIAM B. ROSSOW

Cooperative Remote Sensing Science and Technology Institute, City College of New York, New York, New York

(Manuscript received 3 December 2015, in final form 3 June 2016)

ABSTRACT

Clouds associated with extratropical cyclones complicate the well-developed theory of dry baroclinic waves through feedback on their dynamics by precipitation and cloud-altered radiative heating. The relationships between cyclone characteristics and the diabatic heating associated with cloud radiative effects (CREs) and latent heat release remain unclear. A cyclone tracking algorithm [NASA's Modeling, Analysis, and Prediction (MAP) Climatology of Midlatitude Storminess (MCMS)] is used to identify over 10^6 cyclones in 33 years of the ERA-Interim and collect the properties of each disturbance. Considering storm intensity as related to wind speeds, which depend on the pressure gradient, the distribution of cyclone properties is investigated using groups defined by their depth (local pressure anomaly) and the radius of the region within closed pressure contours to investigate variations with longitude (especially ocean and land), hemisphere, and season. Using global data products of cloud radiative effects on in-atmosphere net radiation [the ISCCP radiative flux profile dataset (ISCCP-FD)] and precipitation (GPCP), composites are assembled for each cyclone group and for ''nonstormy'' locations. On average, the precipitation rate and the CRE are approximately the same among all cyclone groups and do not strongly differ from nonstormy conditions. The variance of both precipitation and CRE increases with cyclone size and depth. In larger, deeper storms, maximum precipitation and CRE increase, but so do the amounts of nonprecipitating and clear-sky conditions.

1. Introduction

Cloud processes in extratropical cyclones lie at the intersection of the well-developed theory of dry baroclinic waves and feedbacks on the dynamics by diabatic heating due to radiation and precipitation. The interaction between waves and clouds is a major source of uncertainty in climate and weather prediction (Bony et al. 2006). Baroclinic waves play a key role in the meridional transport of energy and water (Peixoto and Oort 1992), and the effects of cloud heating on these waves and their associated transports are uncertain. Govekar et al. (2014) compared modeled composites of vertical velocity and relative humidity in the vicinity of midlatitude baroclinic eddies with those of reanalyses. They found that the modeled range of dynamical and thermodynamical properties is more restricted than observed. Similarly, in a comparison between reanalyses and a high-resolution model, Catto et al. (2010) found reanalyses had stronger rates of ascent and descent in the regions surrounding a cyclone. Allan and Soden (2007) showed that the variability of tropical precipitation in many models is also much more limited than observed. Wielicki et al. (2002) reported that the observed top-of-the-atmosphere (TOA) radiative energy budget in the tropics is more variable than represented by models. The restricted range of modeled variability may explain why models struggle to simulate the radiative effects of clouds and has motivated several studies focusing on midlatitude cyclone clouds of the Southern Ocean (Bodas-Salcedo et al. 2012; Naud et al. 2013; Mason et al. 2015).

Many climatological studies of extratropical cyclones exist (Hodges et al. 2011; Rudeva and Gulev 2007; Schneidereit et al. 2010; Simmonds 2000; Simmonds and Keay 2000b,a; Sinclair and Revell 2000; Tilinina et al. 2013; Wang et al. 2006) that focus on frequency of occurrence, geometry, duration, intensity (variously defined), and variability. In general, cyclone climatologies emphasize the variety and nature of the phenomena in terms of dynamics (e.g., Hoskins and Hodges 2002, 2005; Simmonds and Keay 2000b), rather than the effect that physical processes may have on the observed distribution of cyclone characteristics. Rudeva and Gulev (2007)

Corresponding author address: J. B. Polly, City College of New York, 160 Convent Avenue, Steinman Hall, Room 512, New York, NY 10031.
E-mail: jpolly00@citymail.cuny.edu

DOI: 10.1175/JCLI-D-15-0857.1

established simple and useful relationships that capture changes in size as a function of cyclone lifetime. A similar model relating cyclone depth (with a definition different than ours, defined later) to lifetime was developed by Schneidereit et al. (2010). Deviations from these relationships are attributed to rare, intense, and long-lasting events; however, it is these events that most severely impact people and property, so it is critical to understand why they exist and what distinguishes these events from the majority of cyclones.

The relationships between cyclone dynamical properties and diabatic heating are especially important in the midlatitude regions, where clouds associated with the low-pressure half of transient waves more effectively trap thermal [longwave (LW)] radiation within the troposphere compared with the high-pressure half of the wave (Tselioudis et al. 2000). The net modulation of the transient waves by this differential effect remains unclear, although Tselioudis and Rossow (2006) have shown that the intensity of a cyclone is positively correlated with the magnitude of the net TOA radiative heating and cooling by LW and shortwave (SW) cloud radiative effect (CRE), respectively. In a study of Southern Ocean cloud regimes, Haynes et al. (2011) demonstrated the climatological importance of extratropical cyclone cloudiness by showing that clouds associated with the warm sector (pre–cold frontal) exhibit the largest SW CRE of all SH midlatitude cloud regimes. Mason et al. (2015) found that the cloud regime with the largest net contribution to the modeled SW bias is a shallow frontal cloud regime often observed in cyclone warm fronts, yet infrequently found in models. While this cloud regime is associated with the largest SW bias as a result of its absence from models, Bodas-Salcedo et al. (2012) provided an alternative perspective, showing that the subsiding cold-air regions in and around these SH storms correspond to the greatest positive bias in absorbed SW radiation in the Met Office model. Given the errors associated with cloud regimes, frontal dynamics, and surrounding meteorological conditions, it is important to establish relationships between cyclone properties and the *in-atmosphere* CRE to serve as a reference for models and extend the TOA-only studies of Tselioudis et al. (2000) and Haynes et al. (2011).

Several studies have provided detailed analysis of cyclone cloud structure by constructing spatial distributions of cloud and precipitation properties. Naud et al. (2012) provided horizontal distributions and vertical profiles of warm frontal cloud and precipitation properties, and a similar analysis for cold fronts was presented in Naud et al. (2015). Hemispheric and seasonal differences were identified in each case, and dynamical dependency on moisture, temperature gradient, and vigor of ascent were explored. These, and other similar studies, provide valuable information on the vertical and horizontal structure of cloud, precipitation, and dynamical variables for a subset of cyclones, which aid model evaluation.

Understanding the coupled relationships between cyclone dynamics, their clouds, the earth's radiation budget, and what feedbacks these components have on one another is an issue of considerable scope. A scheme for investigating these issues ought to consist of multiple parts, which together will attempt to extend the previously mentioned studies and address this large-scale challenge. First, it is necessary to investigate the general relationships between cyclone characteristics and the diabatic heating associated with their clouds. To preserve generality of these relationships, it is best to consider all types of cyclones at all stages of their lifetime. Second, using these established relationships, the cyclone lifetime may be considered. In this Lagrangian analysis it will be possible to study the temporal dependence between cyclone properties (e.g., intensity) and diabatic heating. Also the time-integrated heating of the atmosphere by each cyclone may be quantified. Third, the effects of differences in the spatial distribution of heating within the storm must be considered. Having performed the general investigation in the first step, more informed subsetting decisions may be employed at later steps to analyze various types of storms and stages of lifetime.

Here we address step one of the three aforementioned tasks: study the relationships between cyclone properties, intensity, and their cloud-associated diabatic heating using a large sample of storms. We attempt to identify which storms have the greatest contribution to in-atmosphere diabatic heating and, in doing so, build the necessary foundation for assessing the dynamical response of cyclones to changes in the distribution of diabatic heating.

Based on a new, comprehensive database that identifies and tracks cyclone motions (Bauer et al. 2016), we first consider how to characterize the distribution of cyclone strengths. To accomplish this, we do not consider the cyclone life cycle at this stage so that we can examine each occurrence of a cyclone independently. Several quantities by which to distinguish between cyclones have been considered, and various characterization schemes have been compared (section 3). We settle on a simple joint distribution of two properties (section 4) to examine the variations of cyclone properties on intensity (section 4a) and their seasonal and interannual variability (section 4b). Then we composite data products that quantify radiative and precipitation heating of the atmosphere by clouds [sections 4c(1) and 4c(2)] to investigate the correspondence between the

distribution of cyclone attributes and cloud-induced diabatic heating.

2. Cyclone identification and data

A list of many cyclone tracking schemes and a comparison between their features and results is provided by Neu et al. (2013). Differences between algorithms are summarized, and Neu et al. (2013) find general agreement in the well-developed stages of storm lifetime. We use a new cyclone tracking algorithm: the NASA Modeling, Analysis, and Prediction (MAP) Climatology of Midlatitude Storminess (MCMS) described fully by Bauer et al. (2016). MCMS tracks cyclones by the local minimum mean sea level pressure (SLP) identified via a search centered around every grid cell. Details of filtering which SLP minima correspond to actual cyclones, sensitivity tests, and demonstrated agreement of MCMS results with algorithms intercompared in Neu et al. (2013) may be found in Bauer et al. (2016). Hereafter, we refer to an SLP minimum, which has been identified and retained as a ''center,'' meaning the center of a storm. Each center included in the database is a part of a storm lasting (and tracked for) at least 24 h.

MCMS scans the area surrounding each center for the outermost closed contour of SLP and delineates this enclosed area as ''stormy.'' This stormy region is attributed to the center within the enclosing SLP contour; we refer to such centers as ''attributed centers'' (AC). Identification of this stormy region provides an advantage when compositing external quantities by separating stormy and nonstormy information—thus, allowing a better isolated analysis compared to the conventional fixed-map-window approach (cf. Field and Wood 2007; Bodas-Salcedo et al. 2012). Considering the storm area of influence also produces statistics less sensitive to mapping and counting procedures (Bauer et al. 2016). A center's attributed stormy area depends on the spatial resolution of the input data: there exist small perturbations in the SLP field such that an identified center may have no closed surrounding contour of SLP. The frequency of these ''empty centers'' (EC) is dependent on both the horizontal grid resolution and the pressure contour interval size (Bauer et al. 2016).

It is possible for multiple centers, both empty and attributed, to be enclosed by a larger SLP contour: Bauer et al. (2016) refer to this surrounding pressure level as a multicenter contour (MCC). In this case, the area bound by the outermost contour is also considered stormy, and the centers within the MCC are called ''entangled centers'' (NC). As shown in Fig. 1, the set of all centers is AC + EC, and NC $\subset$ (AC + EC). We define the subset of centers that are both attributed and entangled (ANC) as ANC = AC $\cap$ NC. Likewise, the subset of empty centers that are also entangled (ENC) is defined as ENC = EC $\cap$ NC. Note that the majority of centers are NCs and that NC = ANC + ENC.

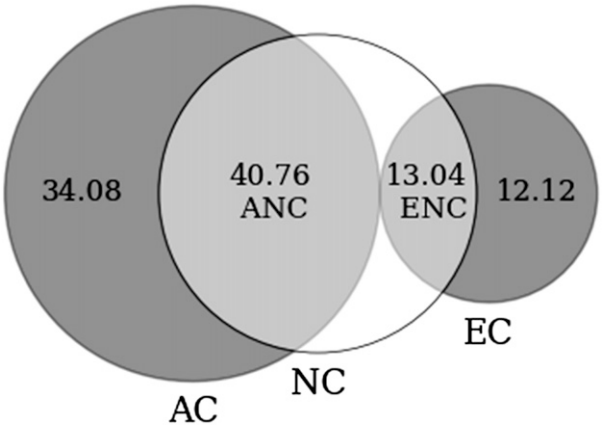

FIG. 1. Venn diagram depicting percentages of center types corresponding to AC, NC, EC, and ANC or ENC. Percentages listed are in reference to all centers prior to collapse of secondary centers with no subsetting by season or property.

MCMS does not assign area or depth (defined in section 3) to ECs, which by definition have no attributed area or surrounding closed SLP contour. To include an EC in our statistics we duplicate properties from the most recent previous time step corresponding to an AC from the same evolving storm. Should the empty center occur as the first identified center in the storm with future ACs, the properties of the chronologically subsequent centers are assigned to the EC. Approximately 1% of empty centers are from evolving systems that are composed entirely of ECs. For this small fraction of centers the minimum values of the entire data record are assigned to each respective property. We use the same procedure to assign depth and radius to ENCs using the depth and radius of the entire entangled region (see below) as an upper limit for the ENC information we assign from other time steps.

Within an MCC, we refer to the NC with the lowest SLP as the ''primary'' center and all other centers within the surrounding MCC as ''secondary'' centers. An example case of primary and secondary center entanglement is shown in Fig. 2. MCMS assigns a depth to the whole stormy region, calculated as the pressure difference between the outermost SLP contour of the MCC and the center pressure of the primary center so that the depth of the stormy region is always greater than the individual depths of the constituent centers. MCMS also assigns an area to the region bound by this MCC.

Stormy regions with multiple centers enclosed by a surrounding pressure contour are given a special treatment,

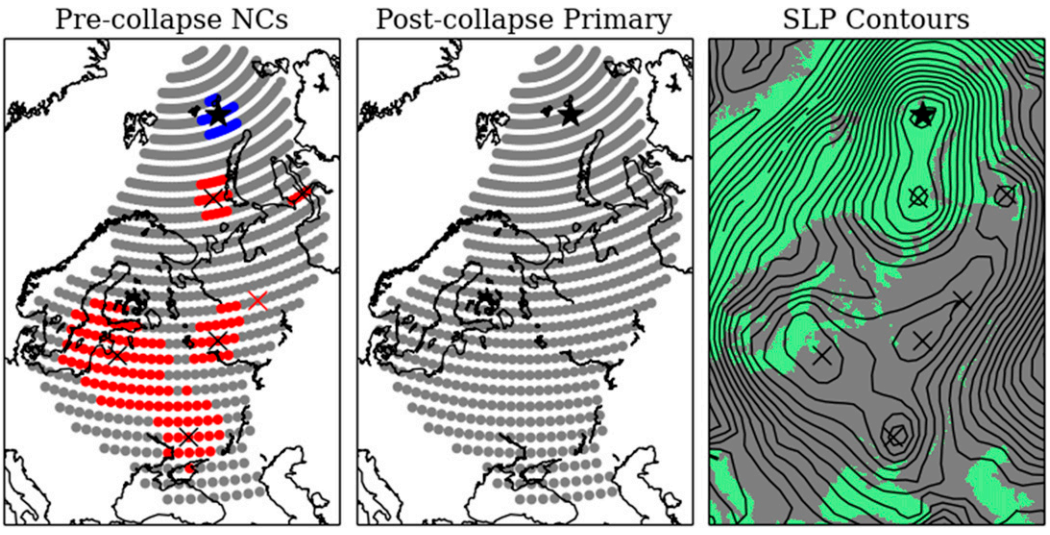

FIG. 2. Example illustrating the collapse of secondary centers onto their respective primary using a 𝔾9 storm located over northern Europe and Scandinavia at 0000 UTC 31 Mar 2012. The primary center (lowest SLP) is denoted with a black star near the panel tops. (left) The stormy region of the primary center is denoted in blue. Five secondary ANCs exist and are marked with a black ×, with each respective stormy region in red circles. One secondary ENC exists, marked with a red ×, and by definition without an associated stormy region. The entire entangled region, enclosed by the outermost SLP contour surrounding all NCs (and outside ANC stormy regions), is denoted in gray circles. (center) All stormy regions and area contributions from secondary centers and the entire entangled region are now associated with—or collapsed onto—the primary center. (right) Associated SLP contours.

which is consequential to our study. We ''collapse'' the secondary NCs onto the primary NC for the analyses we present. This simply assigns the depth and equivalent radius of the entire region enclosed by the MCC to the primary center, treating it as a single entity. The radius we assign to the primary center is derived from the area contributions of the ANCs and the stormy region within the MCC, the latter defined as the region within the MCC but outside of the ANCs. Thus, the area footprint assigned to the primary center preserves the sum of all collapsed center footprints, the stormy region between centers, and the primary center itself. We provide details and justification of this decision in the appendix and demonstrate that secondary centers are both smaller and shallower than their associated primary centers.

The SLP field used for tracking is the ERA-Interim (ERAI) product described in Dee et al. (2011). It is 6 hourly with 1.5° latitude by 1.5° longitude grid size, for the years 1979–2012. All results contained herein were also computed for the National Centers for Environmental Prediction (NCEP)–U.S. Department of Energy (DOE) AMIP-II reanalysis (R-2; Kanamitsu et al. 2002), which is also 6 hourly, but coarser resolution at 2.5° latitude by 2.5° longitude. In both reanalyses the meridional extent of our study spans from 15°N–S to the respective poles of each hemisphere. Aside from differences in number of cyclones (mainly ECs) detected due to horizontal grid resolution, as observed in, for example, Tilinina et al. (2013), differences between R-2 and ERAI are only appreciable in the interannual variability results that follow and will be further discussed in section 4.

Composites of radiation and precipitation heating of the atmosphere are constructed using the spatial information defined by the stormy regions of either ACs, primary NCs, or a single grid box in the case of an EC. Radiation data are provided by the International Satellite Cloud Climatology Project (ISCCP) radiative flux profile dataset (ISCCP-FD; Zhang et al. 2004), which contains both SW and LW flux profiles at 3-hourly increments with global coverage for July 1983 through 2009. ISCCP-FD is mapped on an equal-area grid with equatorial resolution approximately equal to 2.5°. Fluxes are available at the surface (SRF) and TOA and at three other vertical levels. Upwelling and downwelling fluxes are available at these levels for clear-sky and full-sky conditions. We calculate in-atmosphere net fluxes as the difference of net TOA and net SRF fluxes. This differs from most other studies reporting CRE using TOA information only (e.g., Tselioudis and Rossow 2006; Haynes et al. 2011). The total flux into the atmosphere from both LW and SW components is reported for both clear-sky and all-sky (including cloud) cases. To determine the CRE, we subtract the clear-sky from the all-sky case, resulting in the cloud component of the in-atmosphere radiative flux divergences.

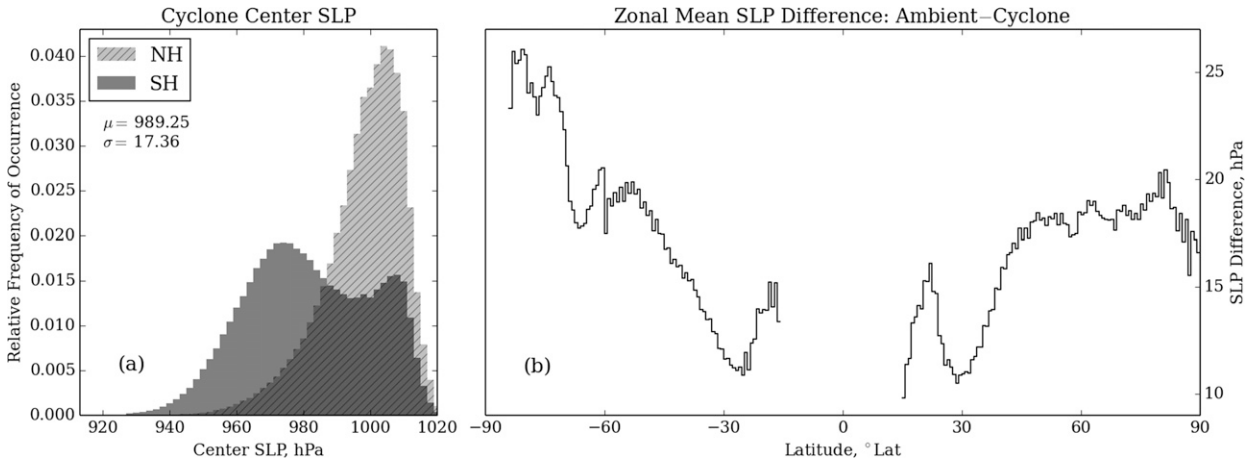

FIG. 3. Cyclone center (a) SLP distributions for SH and NH with global mean μ and standard deviation σ, and (b) the difference between zonal means of SLP and cyclone center SLP.

Precipitation data are provided by the Global Precipitation Climatology Project (GPCP; Huffman et al. 2001), which provides daily estimates of precipitation with global coverage at 1° equal angle resolution (1-Degree Daily Combination, version 1.2). GPCP is constructed using a combination of both gauge and satellite estimates and is available from October 1996 through the present. In these composites we retain precipitation estimates equal to zero and note that our findings are qualitatively similar when zero precipitation values are omitted. GPCP provides estimates at daily time intervals, while the ERAI we use for cyclone tracking has 6-hourly intervals. Consequently, some precipitation values may be composited multiple times if a storm's area of influence exists in the same location for multiple time steps (e.g., a slow-moving storm). We address this issue by counting the number of times a cyclone's area passes over any location and dividing the precipitation measurement at that location evenly among all of the cyclones that pass over that location. We performed the analysis with and without this "splitting" technique but found no qualitative difference in results. Thus, we choose to allow daily values to be composited multiple times by the same or more than one cyclone.

In what follows, when discussing the properties of centers, we include results for the whole period 1979–2012; but when discussing the composite diabatic heating, the results are only for the period common to GPCP and ISCCP-FD (1997–2009).

3. Distribution of cyclone attributes

Cyclones identified by MCMS have several properties (not all of which are employed in this study), including the radius, depth, and center pressure. We also calculate an SLP anomaly and a geostrophic wind speed proxy. These five properties form the basis of the statistical analysis we present.

The distribution of SLP for all centers is shown in Fig. 3a, separated by hemisphere. The hemispheric differences in cyclone center SLP are, to first order, due to hemispheric differences in the mean SLP field. Zonal mean cyclone center SLP closely follows the zonal means of the entire SLP field, though offset ~16 hPa lower, as shown in Fig. 3b. Differences between the zonal means are largest in the polar regions, especially in the Southern Hemisphere (SH) near the Antarctic Plateau. This is likely because of an assumed lapse rate in the reduction of surface pressure to sea level in the presence of topography. Away from the poles the difference between zonal mean SLP and the cyclone-only component is similar in both hemispheres. Thus, center SLP is not an intrinsic property of the cyclones and does not allow hemispheric (or seasonal) comparisons of cyclone strength. Furthermore, it has been shown by Benestad and Chen (2006) that SLP is not well correlated with geostrophic wind speed in the vicinity of the center.

Some type of SLP anomaly (SLPA) is commonly used to quantify the strength of a cyclone as a deviation from some mean state. Here we calculate SLPA as a difference between a 2-week moving-window average of the SLP field at each location and the cyclone center pressure to better isolate synoptic variability (shown in Fig. 4a). Defined in this way, a positive anomaly corresponds to a larger deviation from the mean and thus a stronger disturbance. Compared with SLP there is less hemispheric difference between Northern Hemisphere (NH) and SH distributions; however, it is difficult to interpret SLPA in terms of cyclone intensity because it is

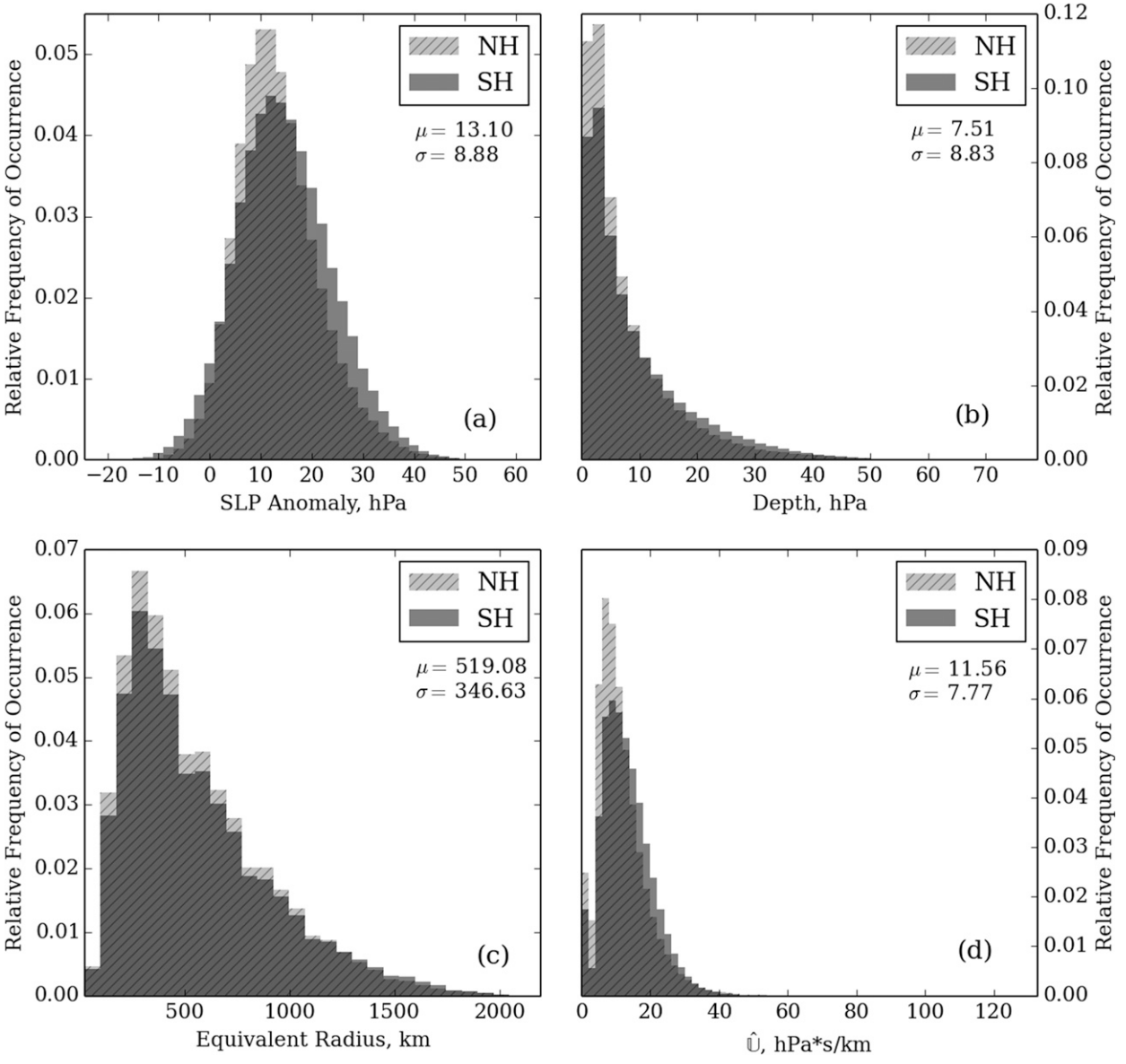

FIG. 4. The NH and SH distributions for cyclone center (a) SLPA, (b) depth, (c) equivalent radius, and (d) $\hat{U}$. The means μ and standard deviations σ correspond to the global distributions of each.

complicated by a sign ambiguity. Lower center SLP is simply interpreted as a stronger storm; however, SLPA can be either positive or negative. Negative SLPA occurs when cyclone center SLP is higher than the collocated time-average SLP, which may correspond to a region of high cyclone activity or persistent low pressure. Though the SLPA approach better isolates synoptic variability, the background state is still contaminated by hemispheric and seasonal differences, persistent regimes of high and low pressure, and errors associated with reduction of surface pressure to sea level in high-altitude regions. Furthermore, the nonlocal temporal information used in calculating the anomaly can misrepresent the instantaneous strength of a given disturbance. Consequently, the anomaly is an unclear gauge of cyclone intensity in a global intercomparison of cyclones.

Pressure depth (henceforth depth) serves as a metric of intensity or strength (as we discuss below) and is calculated for each AC as the pressure difference between the outermost closed pressure contour surrounding only that center and the SLP of the center itself. Depth defined in this manner is a unique characteristic of MCMS and describes the cyclone's deviation from the surrounding ambient pressure field. Resolution of the

reanalyses indirectly influences the depth calculation by means of the center finding procedure. MCMS locates SLP minima by fitting a paraboloid to the gridded SLP field, where the nadir specifies the center location and center pressure with a precision finer than either horizontal grid resolution or pressure discretization. Thus, depth values are calculated with precision greater than 2 hPa but are reported as the nearest multiple of 2 hPa with a minimum allowable depth of 0 hPa and a maximum value of 72 hPa, where a depth of zero simply corresponds to centers with ''very small'' depth. Our comparisons of MCMS results when applied to different reanalyses (not shown) suggest that, while depth depends on resolution, there are no qualitative differences in the distribution or range of values observed.

Depth is a positive local quantity and is not hemispherically biased (Fig. 4b). The depth distribution can only be interpreted one way (unlike SLPA): larger depth values correspond to a greater difference between the outermost closed SLP contour surrounding the cyclone center and the center pressure. Compared with SLPA, the geometric and physical interpretation is clearer. While there may be hemispheric differences and a range of values as a result of the maturation and decay of cyclones themselves, the depth measurement itself does not depend on a seasonally varying or regionally dependent reference state.

An area-equivalent radius (henceforth radius) is assigned to each AC identified by MCMS. Using the outermost closed SLP contour, the algorithm computes the area contained in this contour and projects a circle of equal area on the geoid centered at the latitude of the corresponding SLP minimum. The area-equivalent radius is the radius of this projected equivalent-area circle [see Bauer et al. (2016) for details]. This projection method yields radius values ranging from 22 to 2208 km, with discretized interval spacing depending on reanalysis resolution. As shown in Fig. 4c, there are negligible differences in distribution of radius between hemispheres.

All of the classifications and analyses presented below were done using SLP, SLPA, and depth. We find that, compared with SLP-based metrics, the depth provides a cleaner description of the cyclone centers by more accurately describing cyclone behavior as a perturbation from the local state. Depth is a property that is not influenced by season, location, or other nonlocal information that contaminates the other metrics.

An additional intensity metric was explored that is similar to the geostrophic wind intensity metric in Benestad and Chen (2006), but simplified. Geostrophic balance imposes a fluid velocity constraint proportional to the gradient of the pressure ∇p. We approximate the magnitude of the local pressure gradient by substituting MCMS reported depth D and radius R such that $|\nabla p| \approx D/R$ and calculate a geostrophic wind speed proxy $\hat{\mathbb{U}}$ as

$$\hat{\mathbb{U}} = \frac{1}{10 f \rho} \frac{D}{R}, \tag{1}$$

where ρ is density, and the Coriolis parameter is $f = 2\Omega \sin\phi$, in which ϕ is the cyclone center latitude and Ω is the earth's rotation rate, approximately 7.292×10^{-5} rad s^{-1}. We assume a constant density at the surface of 1.235 kg m^{-3} and apply a scaling factor of 0.1 to give the units of $\hat{\mathbb{U}}$ in meters per second.

Despite the dependence on latitude, distributions of $\hat{\mathbb{U}}$ are nearly identical between hemispheres, as shown in Fig. 4d. Distributions for both hemispheres contain extreme values in the tails of each histogram, but NH cyclones are more frequent for less intense values. NH cyclones are also more frequent for shallower values of depth, and similarities between distributions of depth and intensity suggest that depth is the governing quantity in the formulation of $\hat{\mathbb{U}}$ (as we show below). Note, however, that the effect of the Coriolis parameter is nonnegligible, resulting in amplification of $\hat{\mathbb{U}}$ at lower latitudes.

The conventional definition of a strong storm is increased surface winds and optically thick clouds accompanied by intense precipitation (Houze and Hobbs 1982; Lau and Crane 1995; Field and Wood 2007). There exists a broad range of intensities among all identified storms, and to investigate the relationship between cloud-associated diabatic heating and storm intensity, we seek a combination of properties that allow for objective discrimination. Radius and depth contain only local spatiotemporal information and, compared with SLP, are better suited for a global intercomparison of cyclones. Since $\hat{\mathbb{U}}$ depends linearly on both radius and depth, the same value of $\hat{\mathbb{U}}$ may be produced by different combinations of each. Thus, we use the joint distribution of depth and radius to describe changes in the distributions of cyclone centers, while using $\hat{\mathbb{U}}$ to explicitly quantify intensity for each cyclone.

Individual distributions of depth and radius are skewed monomodal shapes (Figs. 4b,c), and a three-group representation captures this structure. To monitor the shape of the joint distribution, we divide the individual distributions of each property into terciles (33rd and 66th percentiles are used for separation). Performing this separation using each dimension separately does not predetermine the shape of the 2D distribution. Depth and radius as defined have a resolution-dependent lower bound but no imposed upper bound. The depth metric is reported at 2-hPa intervals, which makes partitioning the distribution more sensitive to the type of inequality condition assigned at the thresholds. To evenly distribute

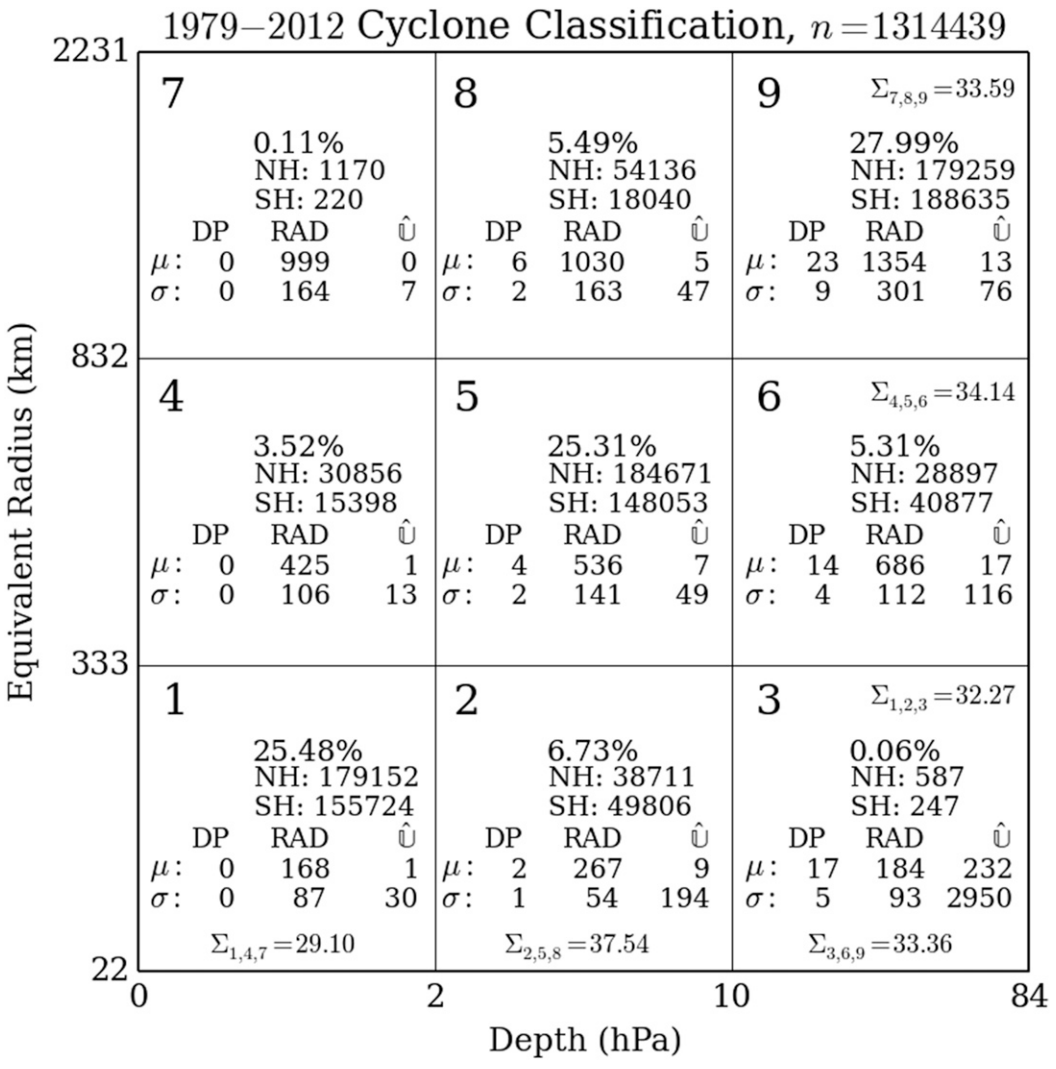

FIG. 5. Nine-fold group schematic using radius and depth. Note that tercile thresholds are not drawn to scale. Descriptions of population subset within each group pertain only to the subset within each bi-interval. Counts of NH and SH centers are given for each group, as well as mean μ and standard deviation σ of cyclone center depth (hPa), radius (km), and $\hat{\mathbb{U}}$ ($\mathrm{m\,s^{-1}}$). Corresponds to after collapsing secondary NCs onto a single primary NC.

the population among three subsets, we employ a strictly less (greater) than condition for inclusion in the lowest (highest) tercile. The distribution of cyclone characteristics is represented by nine groups in the joint depth–radius distribution.

4. Results

In this paper, cyclone centers are assigned to groups based on their individual properties without consideration of duration. The geographic, seasonal, and interannual variability of these groups is examined. Finally, we present composites of radiation and precipitation associated with each of the radius–depth groups.

The joint histogram in Fig. 5 includes all center types, with EC treatment performed as described in the preceding section, and with secondary centers having been collapsed onto their respective primary center. The nine groups (thresholds demarcating groups not drawn to scale) are not equally populated—approximately 79% of all centers are within groups 1, 5, and 9 (hereafter, the $\mathbb{G}X$ notation is used to indicate group X)—indicating a strong correlation between depth and size, as has been reported in other studies (Rudeva and Gulev 2007; Simmonds 2000). Groups become less populated away from the diagonal formed by $\mathbb{G}1$, $\mathbb{G}5$, and $\mathbb{G}9$. Centers in off-diagonal groups are not distinct ''clusters'' of points in depth–radius space, but correspond to the tails of each

distribution (see Figs. 4b,c). The least frequent cases correspond to very large, very shallow centers (𝔾7) and very small, very deep centers (𝔾3). Because of the low frequency of these centers, we will generally disregard 𝔾3 and 𝔾7 in discussing results.

The correlation between depth and radius is sensitive to how each property is defined. It has been shown that cyclone radius depends on lifetime and intensity [as defined in Rudeva and Gulev (2007)] and that radius increases as cyclones evolve (Simmonds 2000; Grotjahn et al. 1999). However, Schneidereit et al. (2010) found that, over the lifetime of the cyclone, changes in size were negligible compared to changes in depth (different from our definition), with no coherent behavior between the two properties. We comment that the difference in these conclusions is perhaps due to differing definitions of radius, depth, and intensity. Rudeva and Gulev (2007) calculate an effective radius from a virtual circumference constructed by searching radially outward from the cyclone center for a zero-value SLP gradient. Alternatively, Schneidereit et al. (2010) fit an azimuthally symmetric Gaussian function (centered on the cyclone center) to the surrounding geopotential height field and then define radius as the standard deviation of the Gaussian. The definition of radius we use here more closely resembles that used by Rudeva and Gulev (2007); however, the depth we use geometrically resembles that of Schneidereit et al. (2010). The correlation we observe suggests that a change in one property is accompanied by a proportional change in the other.

In both dimensions, the largest intergroup variances correspond to the larger and deeper 𝔾9 centers, which is the most frequently occurring group. This group has no upper bound in either dimension, and the long tails of each distribution are responsible for the interval size and increased variance.

a. Intensity associated with depth and radius

Statistics of radius, depth, and intensity ($\hat{\mathbb{U}}$) associated with each group are given in Fig. 5. The smallest, deepest 𝔾3 centers have a mean intensity that is more than an order of magnitude larger than any other group. The mean intensity of 𝔾3 centers is not an accurate physical wind speed and is amplified by the Coriolis parameter at low latitudes. We have found that 𝔾3 centers are mostly associated with long-lasting tropical cyclones that have meandered outside the tropics. A few 𝔾3 centers are however associated with the maximum intensity in the lifetime of an extratropical storm.

The diagonal formed by 𝔾1, 𝔾5, and 𝔾9 separates the joint distribution as less intense groups lie on the larger, shallower side (𝔾4, 𝔾7, and 𝔾8), while more intense groups exist on the smaller, deeper half (𝔾2, 𝔾3, and 𝔾6). On the diagonal itself, mean values of intensity increase, moving toward larger and deeper groups, showing that intensity is well correlated with size and depth. The relative change in depth between groups moving from 𝔾1 toward 𝔾9 is larger than the relative change of radius, showing that changes of depth are dominant in changes of intensity.

Considering groups of similar depth and varying radius (𝔾2, 𝔾5, and 𝔾8), the mean depth increases while mean intensity decreases for progressively larger groups (shown in Fig. 5). However, these groups have roughly equivalent intensity mode values (Fig. 6a). Analogously, groups of similar radius and varying depth (𝔾4, 𝔾5, and 𝔾6) exhibit increasing mean radius for progressively deeper groups. Distributions of $\hat{\mathbb{U}}$ for this combination of groups are shown in Fig. 6b and clearly illustrate the dependence of intensity on depth.

Because of the skewed distribution shapes of both depth and radius, the variance associated with each depth–radius group is positively correlated with that group's mean of these properties and influences the $\hat{\mathbb{U}}$ distributions. Groups that have no upper bound in one dimension (𝔾7, 𝔾8, 𝔾6, and 𝔾3) or both dimensions (𝔾9) correspond to the tails of the individual depth and radius distributions. Given the definition of $\hat{\mathbb{U}}$, it is clear that the extreme tail of the size distribution—in combination with the restricted interval of depth—gives relatively low values of $\hat{\mathbb{U}}$ for 𝔾8. Similarly, the unrestricted tail of the depth distribution with a limited radius interval allows 𝔾6 to take on relatively large $\hat{\mathbb{U}}$ values.

Figure 6c shows the distributions of intensity for the most populous groups, which correspond to very small and very shallow centers (𝔾1), median radius and depth centers (𝔾5), and very large and very deep centers (𝔾9). Each of these groups have a similar frequency of occurrence; however, the largest and deepest group (𝔾9) contains the tail of both the radius and depth distributions. As a result, this most frequently occurring group has the broadest range of $\hat{\mathbb{U}}$ values and totally dominates the high-intensity tail of the distribution.

b. Variability

1) SEASONAL AND GEOGRAPHIC VARIABILITY

The meridional distribution of the entire center population is consistent throughout all seasons and distinctly different for each hemisphere (not shown). The SH has a sharp frequency peak near 60°S, and the NH peak near 50°N is broader. Frequency distributions in both hemispheres skew slightly poleward in warmer seasons, but the NH shift is larger. In general, the seasonal fluctuations in the NH are much stronger than in

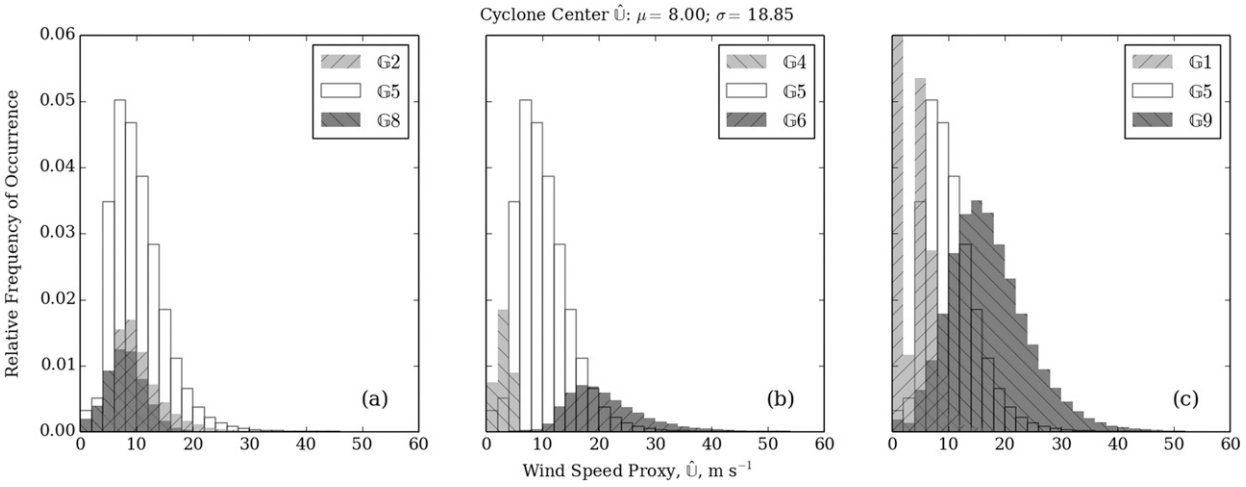

FIG. 6. PDFs of wind speed proxy for different combinations of groups 𝔾: (a) 2, 5, and 8; (b) 4, 5, and 6; (c) 1, 5, and 9.

the SH, and in both hemispheres the largest peak frequency occurs in the fall season.

Considering each depth–radius group reveals that certain groups have an affinity for particular seasons and geographic locations. Meridional distributions separated by season for the most populous groups (𝔾1, 𝔾5, and 𝔾9) are shown in Fig. 7. These are zonal means of center frequency only and do not account for the attributed area, though this does not alter the nature of the results. Each group distribution is represented with frequencies relative to the entire center population, and thus the area under each curve integrates to the overall frequency of that group (shown in Fig. 5). The geographic distributions of these most populous groups 𝔾1, 𝔾5, and 𝔾9 are shown in Fig. 8 without any separation by season. We compute geographic relative frequency of occurrence (RFO) using the stormy regions attributed to each center (as described in section 2), which are less sensitive to details of the center counting procedure (Bauer et al. 2016). Calculation of cyclone center density (or an analogous quantity) and the associated sensitivity to the method are discussed in Bauer et al. (2016), Hoskins and Hodges (2002, 2005), Simmonds and Keay (2000a), Wernli and Schwierz (2006), and elsewhere. The RFOs shown in Fig. 8 (and later for off-diagonal groups) are each scaled by the maximum frequency occurring within each group–hemisphere map. Thus, there is a maximum value of unity in each map, illustrating the locations of each group regardless of relative frequency. Similar zonal means and geographic distributions corresponding to off-diagonal groups (𝔾2, 𝔾4, 𝔾6, and 𝔾8) are shown in Figs. 9, 10, and 11.

Smallest, shallowest centers (𝔾1) show an annual cycle in the NH with peak frequency during warm seasons and minimum frequency during cool seasons (Fig. 7). 𝔾1 centers are primarily located over land and coastal regions. Among other locations, NH peak frequencies occur in the upstream portions of the Atlantic and Pacific storm tracks (Fig. 8). In the SH, these centers show no seasonal variability for latitudes poleward of 40°S, and equatorward of this zone only the cool season shows a reduced RFO. SH peaks are isolated near the southern coasts of Africa, South America, and Australia. In both hemispheres and for all seasons the frequency of these centers peak at lower latitudes.

Figure 7 shows the largest zonal frequency peaks are for the largest, deepest centers of 𝔾9, which in the SH are concentrated near 60°S and show little fluctuation with season. In lower SH latitudes there is a small frequency increase for cool seasons that nearly disappears in summer. Significant seasonal variability is exhibited by the NH 𝔾9 centers, which vary both in frequency magnitude and location of the peak. Lowest peak frequency for NH 𝔾9 occurs in summer, and as summer transitions to fall the location of the peak remains at approximately 55°N but is raised to the greatest magnitude of any season. The location of the frequency peak for NH 𝔾9 centers is most poleward in the fall and summer seasons. Cold season and spring have a frequency peak extending to lower latitudes with an intermediate magnitude.

The RFO distributions in Fig. 8 highlight differences in surface-type preference for 𝔾1, 𝔾5, and 𝔾9, showing the smallest, shallowest storms exhibiting affinity for land and the largest, deepest storms concentrated over oceans. Note that 𝔾5 exhibits a mixture of characteristics found in other groups and—by design—serves as a buffer between distinct regimes. The frequency peak of 𝔾1, 𝔾5, and 𝔾9 occurs progressively further downstream in the NH storm-track regions. This suggests that the

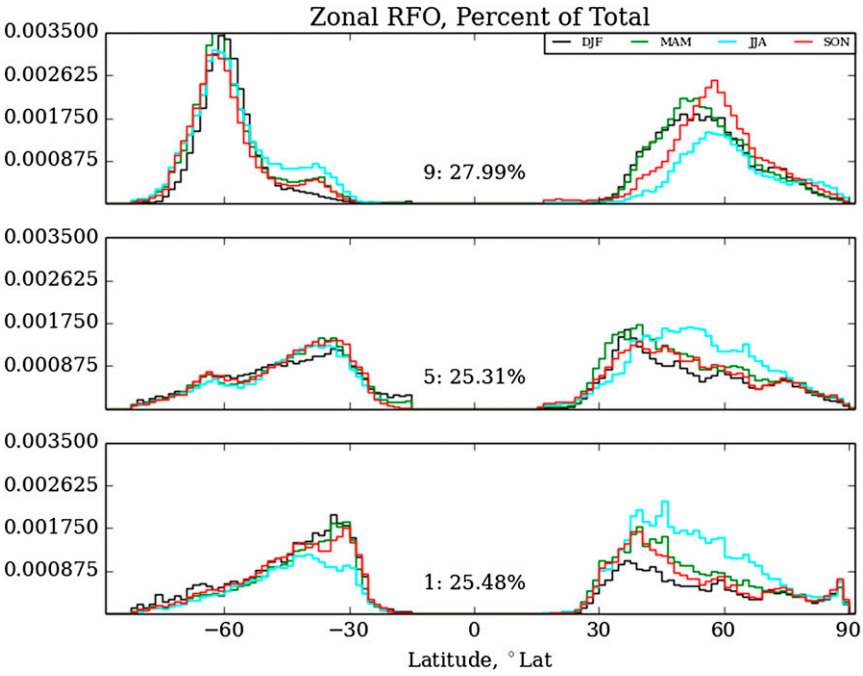

FIG. 7. Zonal RFO of cyclone centers separated by season—DJF (black), MAM (green), JJA (cyan), and SON (red)—for the most populous groups (bottom) $\mathbb{G}1$, (middle) $\mathbb{G}5$, and (top) $\mathbb{G}9$. Integrated frequency beneath each group–season distribution represents that group–season combination's frequency out of the all-season total center population.

groups capture some component of storm development over its lifetime, which will be of interest in our later studies.

Less frequent groups exhibit a seasonal preference depending on which side of the group 1–5–9 diagonal they exist (Fig. 9). Larger, shallower centers ($\mathbb{G}4$ and $\mathbb{G}8$) prefer warm seasons and land, appearing in the vicinity of orographic features, as shown in Fig. 10. Among off-diagonal groups, NH $\mathbb{G}8$ centers show the greatest seasonal change in frequency amplitude and peak location. $\mathbb{G}8$ centers prefer the lee regions of mountain ranges in both hemispheres. In the SH, the zonally elongated frequency distribution of $\mathbb{G}8$ suggests a propagating transient feature, in contrast to several isolated $\mathbb{G}4$ frequency concentrations, which suggest stagnation or subsequent group transition.

NH $\mathbb{G}4$ centers also exhibit a warm season preference; however, the seasonality is weaker than $\mathbb{G}8$ (Fig. 9). Isolated concentrations of $\mathbb{G}4$ centers exist in desert regions (e.g., the Sahara in northern Africa and the Karakum east of the Caspian Sea). This suggests that some of these centers may be nonpropagating heat lows. In the SH, $\mathbb{G}4$ centers are found in the lee of the Andes and off the southern coast of Africa, with peak frequency in austral summer. Frequency peaks near the lee side of the Andes for both $\mathbb{G}4$ and $\mathbb{G}8$ exist on the land surface, near the mountain range (Fig. 10). Hoskins and Hodges (2005) identify a subset of storms originating in this region, and the frequency peaks for both $\mathbb{G}4$ and $\mathbb{G}8$ closely resemble the cyclogenesis locations of the subset of storms they consider (and is further discussed below).

On the smaller, deeper (and intense) side of the group 1–5–9 diagonal, $\mathbb{G}6$ exhibits a slightly increased RFO in both hemispheres during cool seasons, while $\mathbb{G}2$ shows very little seasonality (Fig. 9). Combined with the decreased frequency of $\mathbb{G}4$ and $\mathbb{G}8$ in cool seasons, the seasonality we find agrees with that of Simmonds and Keay (2000a), who report greater mean depths in winter. For these intense groups, the NH seasonal variability is not significantly greater than the SH. Figure 11 shows these smaller, deeper centers tend to be oceanic in both hemispheres. Storminess of $\mathbb{G}2$ and $\mathbb{G}6$ occupies the Atlantic and Pacific storm tracks in the NH, and Hoskins and Hodges (2002) identified peak wind speeds in these regions. This agrees with the relatively large $\hat{\mathbb{U}}$ values associated with $\mathbb{G}2$ and $\mathbb{G}6$ (as well as $\mathbb{G}9$, also in the NH storm tracks). In the SH, $\mathbb{G}2$ and $\mathbb{G}6$ frequencies increase downstream of the Andes. Their geographic distribution resembles the trajectory of storms discussed by Hoskins and Hodges (2005, their Fig. 6) which originate in the lee of the Andes, propagating eastward and poleward. Recall that $\mathbb{G}4$ and $\mathbb{G}8$ were found near orography on the land upstream of the peak frequencies for $\mathbb{G}2$ and $\mathbb{G}6$. This suggests that these more intense groups may

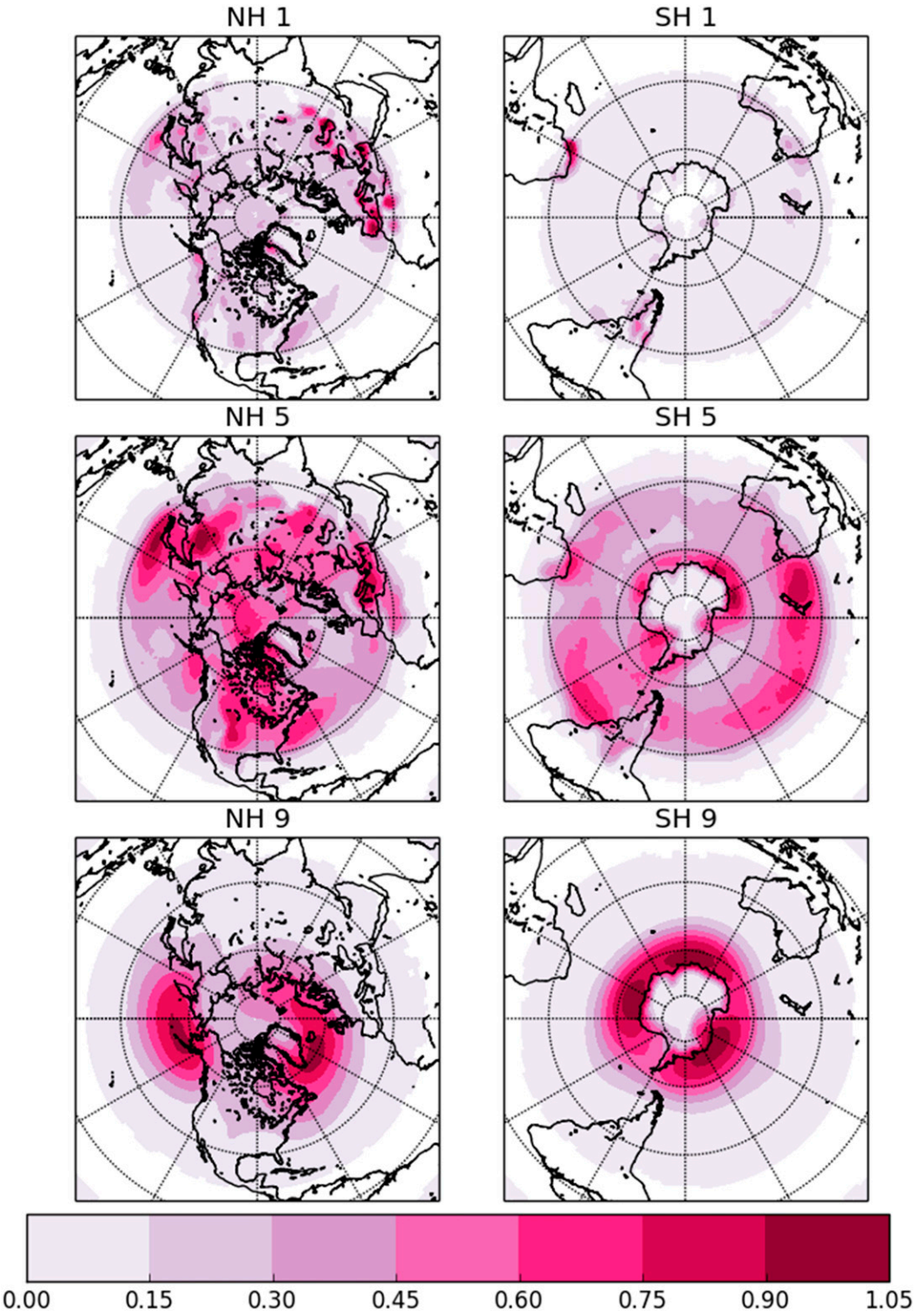

FIG. 8. Scaled RFO of cyclone center attributed (stormy) regions corresponding to the most populous groups (top) $\mathbb{G}1$, (middle) $\mathbb{G}5$, and (bottom) $\mathbb{G}9$ for (left) the NH and (right) the SH. Frequencies are computed without seasonal decomposition and for the entire time record. Each group–hemisphere map is scaled by the maximum frequency occurring within that map so that the maximum value of unity exists in each.

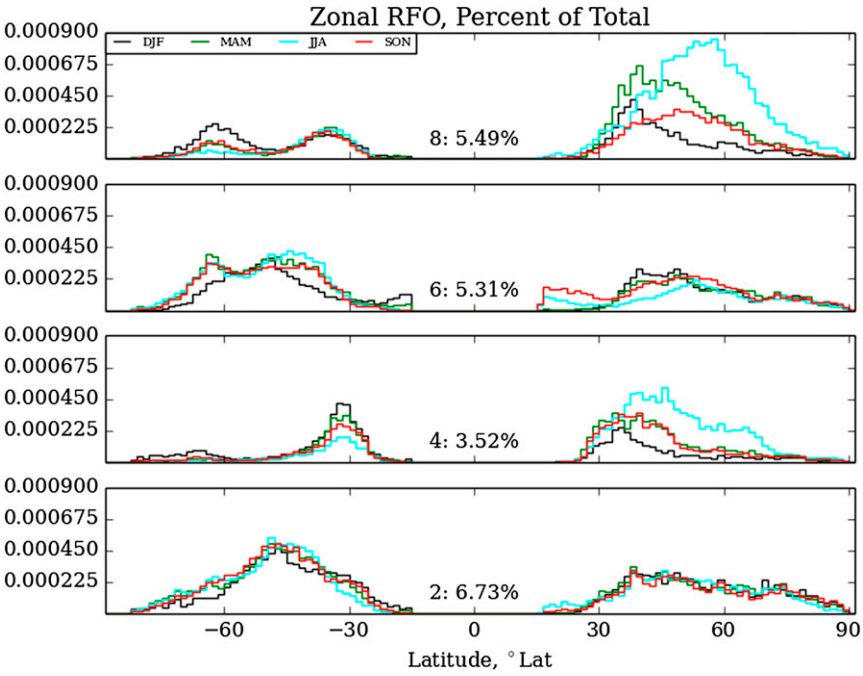

FIG. 9. As in Fig. 7, but for less populous groups (bottom)–(top) 𝔾2, 𝔾4, 𝔾6, and 𝔾8.

capture the mature centers that underwent cyclogenesis in the region adjacent to the Andes and began life as less intense groups.

Summarizing some consistent geographic relationships, to first order we observe the shallowest cyclones (𝔾1, 𝔾4, and 𝔾7) are found over land, while the deepest cyclones (𝔾3, 𝔾6, and 𝔾9) exist over oceans. Cyclones of average depth (𝔾2, 𝔾5, and 𝔾8) are a mixture of both surface types; however, they exhibit a ''second order'' relationship between surface type and radius. Smaller radius storms (𝔾2) are mostly found over oceans, whereas larger storms (𝔾8) are found over land. Cyclones of average depth and radius (𝔾5) are roughly a mixture of both types, reinforcing both the intermediate nature of 𝔾5 centers (as intended) as well as the ability of our depth–radius classification scheme to meaningfully discriminate between cyclone types.

In general, the distribution of centers shifts from the larger, shallower (less intense) side of the diagonal to the smaller, deeper (more intense) side as warmer seasons transition to cooler. Hemispheric differences in seasonal variability have important implications. Compared with the NH, the SH group zonal RFO peaks are less seasonally variable in meridional locations, and the geographic distributions are more zonally symmetric. In the NH, the meridional location of the group peak frequency changes with season, shifting poleward for warmer seasons more strongly for larger groups. There is no such meridional shift of group peak frequency in the SH; rather, different groups remain at a fixed meridional location with seasonally varying frequency amplitude (cf. Figs. 7 and 9). While SH groups themselves do not meridionally shift in season, their superposition can result in a net shift of cyclone properties. For example, Simmonds and Keay (2000a) calculate that the location of the mean SH cyclone radius peak shifts poleward for warm seasons. Our zonal distributions show that the larger SH 𝔾8 centers increase frequency in warm season without a meridional shift in frequency peak, while 𝔾9 centers become less frequent at lower latitudes. The combined effect of the attenuation and amplification of group frequencies can be interpreted as a net poleward shift of properties but is very different from the NH shift of frequencies.

2) INTERANNUAL VARIABILITY

Interannual changes in group RFO are investigated by generating a time series of the yearly fraction of the total center population belonging to combinations of group, season, hemisphere, and center type (e.g., SH, summer, 𝔾5, and ACs). Each point of the time series is calculated as the annual center count corresponding to that combination divided by the time record mean of the same combination. Scaling by the subset mean removes overall frequency differences between subsets. We then consider this RFO time series as an anomaly by computing the difference of the RFO from the time record mean RFO for the same subset. The time series are 33 points in length, each point corresponding to one year of

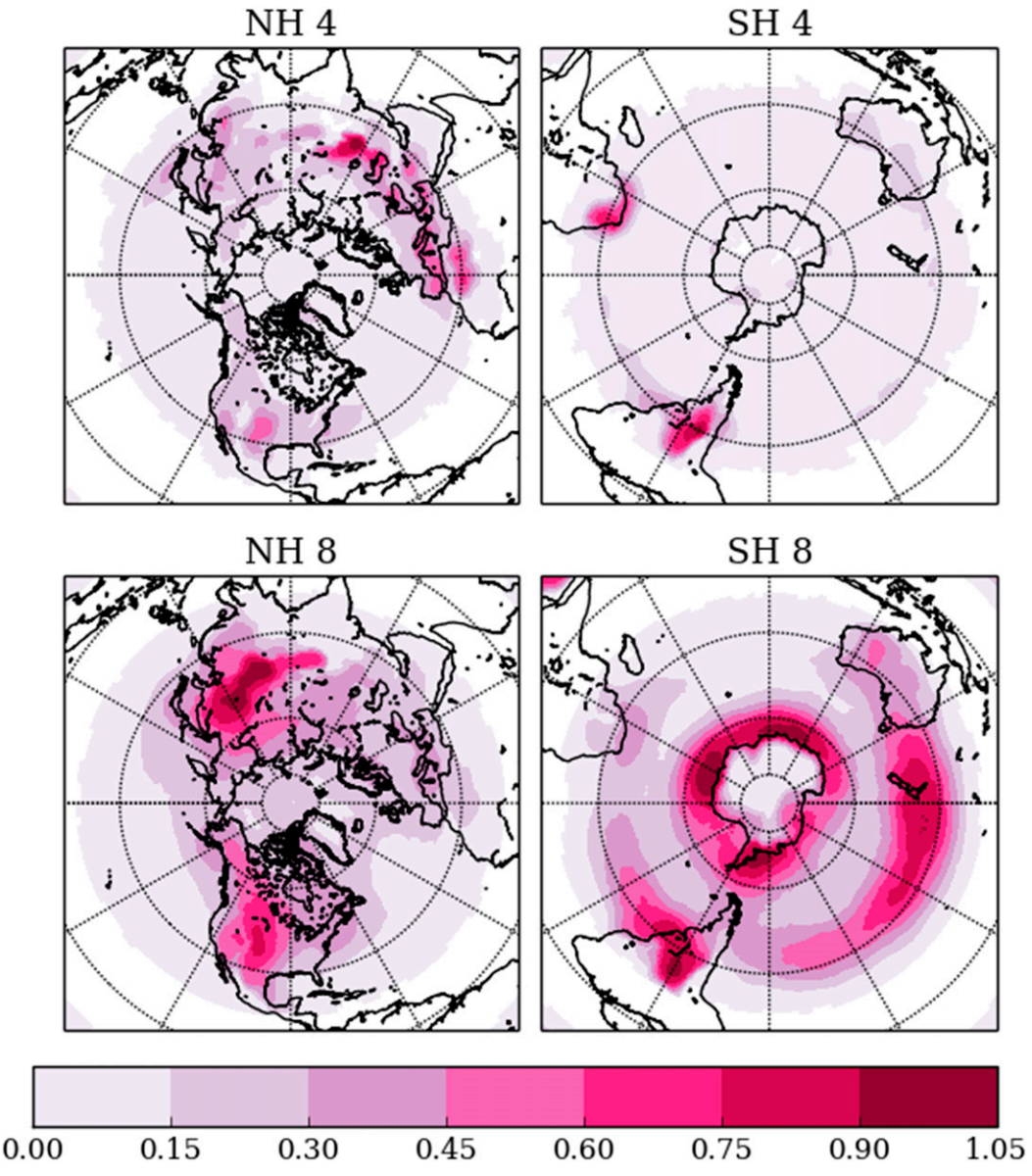

FIG. 10. As in Fig. 8, but for (stormy) regions corresponding to less intense, larger, and shallower groups (top) $\mathbb{G}4$ and (bottom) $\mathbb{G}8$.

the reanalysis. An example of this is shown in Fig. 12 for NH entangled $\mathbb{G}9$ centers.

Cyclone group definitions depend on depth and radius thresholds, which are calculated using distributions for the entire time record. We have considered the possibility that these tercile thresholds themselves change interannually, thus affecting the group populations interannually. We find that threshold values do not significantly fluctuate from one year to the next and are generally equal to the thresholds calculated using distributions for the entire time record. Thus, any interannual changes in group frequency are not attributable to meandering thresholds.

Significance of a systematic change over the record is determined by averaging the RFO anomaly in the first and last thirds of the time record and computing the difference between the mean values in each 11-yr interval (ID). If this difference between the means exceeds the root-mean-square (RMS) error from a linear fit of the entire anomaly time series, then the change is deemed significant—namely, the changes in the signal exceed any noisy fluctuations.

Two reanalysis products are used to study the interannual variability of cyclone centers. A full comparison of tracking algorithm results using multiple reanalysis

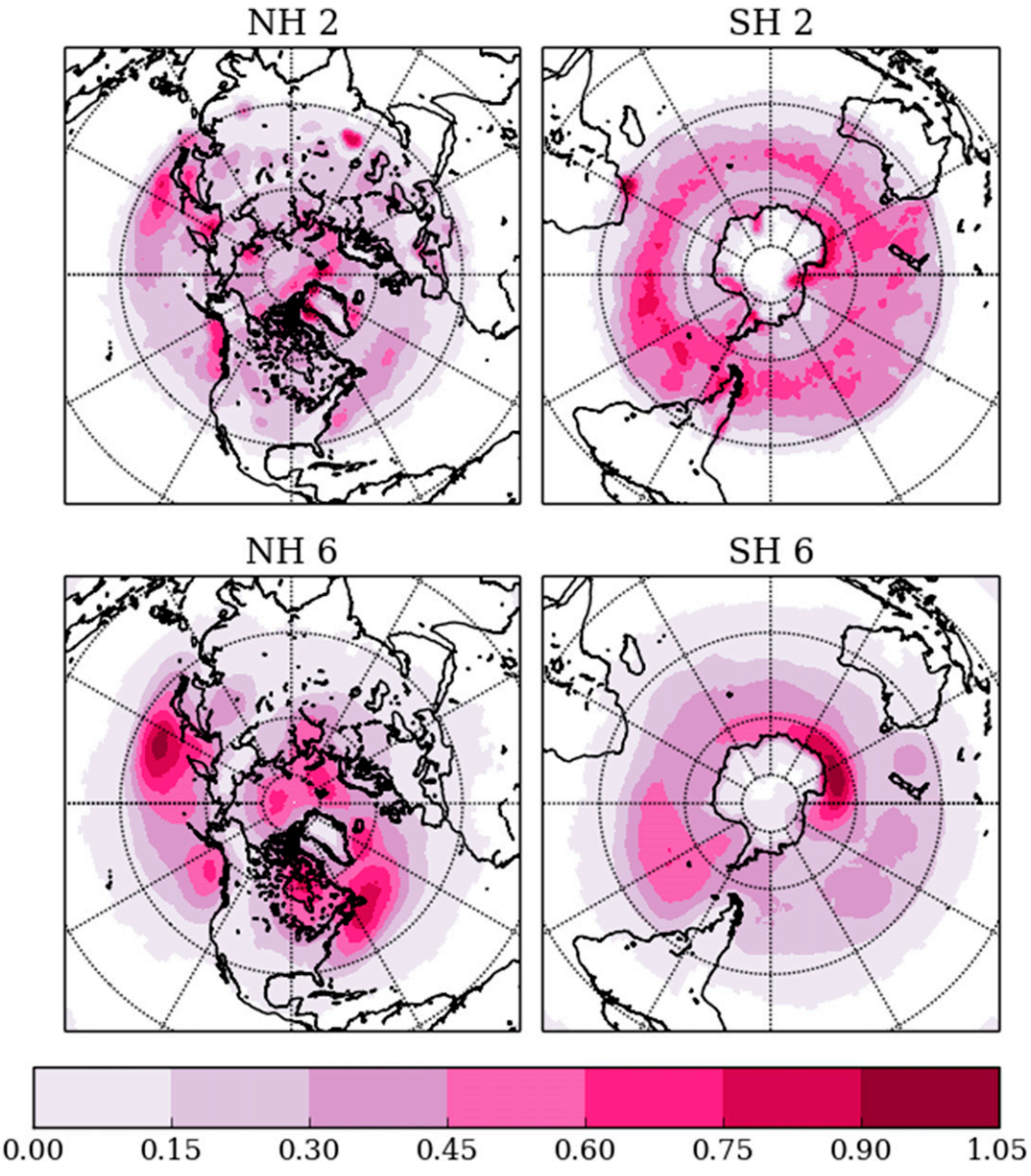

FIG. 11. As in Fig. 8, but for (stormy) regions corresponding to more intense, smaller, and deeper groups (top) $\mathbb{G}2$ and (bottom) $\mathbb{G}6$.

products as conducted by Hodges et al. (2011) is not performed herein but would be a useful future endeavor. To first order, Hodges et al. (2011) find that differences in reanalysis resolution are responsible for many of the differences found between the tracking algorithm outputs. We find significantly more cyclones (mainly ECs) identified in the ERAI because of higher spatial resolution than in the R-2 product. These additional cyclones identified in ERAI are at smaller values of both depth and radius. The maximum radius values detected in the two reanalysis products are nearly identical; however, a greater maximum depth is found for the higher-resolution ERAI. Our intensity metric depends strongly on depth, so this seems to agree with the Hodges et al. (2011) finding that greater intensities are found for higher-resolution products.

We find that the R-2 and ERAI products contrast in the degree of interannual variability over the time record in question. Compared to ERAI, the R-2 exhibits many more significant interannual increases and decreases. Aside from differences that are directly related to spatial resolution, this differing variability between the two products is the strongest difference we observe between them.

We investigated the interannual variability of all center types and combinations of each center type with

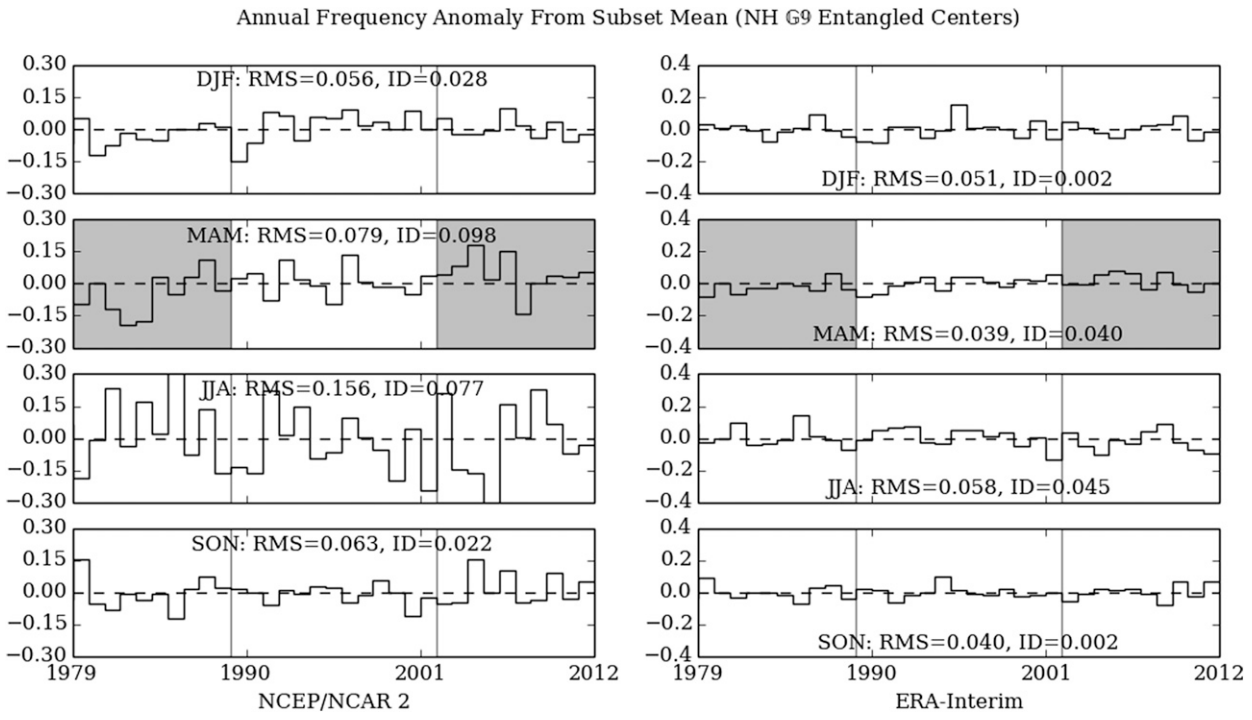

FIG. 12. An example of interannual variability expressed as an anomaly from a time record mean corresponding to subsets of $\mathbb{G}X$, season, hemisphere, and center type combinations (NH $\mathbb{G}9$ NCs shown): (top)–(bottom) different seasons and (left) R-2 and (right) ERAI. Shading denotes "significance" when mean anomaly difference between the first and last 11-yr intervals exceeds the RMS error of the entire time series.

permutations of hemisphere, season, and group. Despite many significant interannual changes found in the R-2 product, only one combination was found to have a significant trend in both the R-2 and ERAI reanalyses. Both products agree on an increase of the largest, deepest ($\mathbb{G}9$) NH springtime (March–May) entangled centers, as shown in Fig. 12. While both reanalyses agree on this subset of centers exhibiting some interannual change, the anomaly time series themselves are dissimilar. Furthermore, aside from this subset there is essentially no agreement on interannual variability between these products when considering the various combinations of center type, hemisphere, season, and depth–radius group.

c. *Cloud radiative effect and precipitation*

We represent the in-atmosphere diabatic heating due to cloud processes associated with each cyclone center via composites of precipitation and the net in-atmosphere CRE. Many studies focus on CRE at TOA (Tselioudis and Rossow 2006; Haynes et al. 2011), which does not fully capture the effects of clouds within the atmosphere itself. Composite statistics assembled from these measurements are analyzed with respect to their depth–radius group as in the preceding analysis, but for 1997–2009. We introduce an additional group to better understand the difference between areas that are associated with a cyclone and those that are not. The group $\mathbb{G}0$ is defined as all regions not associated with a cyclone, excluding 30°N–30°S.

Given that the domain of $\mathbb{G}0$ is simply all regions outside of the SLP contours surrounding each cyclone center, this does not mean that $\mathbb{G}0$ is exclusively a fair weather regime: the influence of an extratropical cyclone in the form of frontal features will often extend beyond this outermost SLP contour (Bauer et al. 2016; Catto and Pfahl 2013). Thus, some cyclone-associated diabatic heating will occur within $\mathbb{G}0$. Catto and Pfahl (2013) quantify the frequency of extreme precipitation events associated with fronts, stormy regions, or a combination of the two. Despite the presence of "remote fronts" associated with a low-pressure feature, outside the stormy region, Catto and Pfahl (2013) find the majority of extreme events are explained by coinciding frontal and low-pressure features. Thus, our method of compositing using the cyclone's stormy region captures a significant portion of the cloud and precipitation features associated with a storm, and, to first order, $\mathbb{G}0$ can serve as a nonstormy regime.

Within the region associated with each individual cyclone center there are usually multiple values of precipitation and

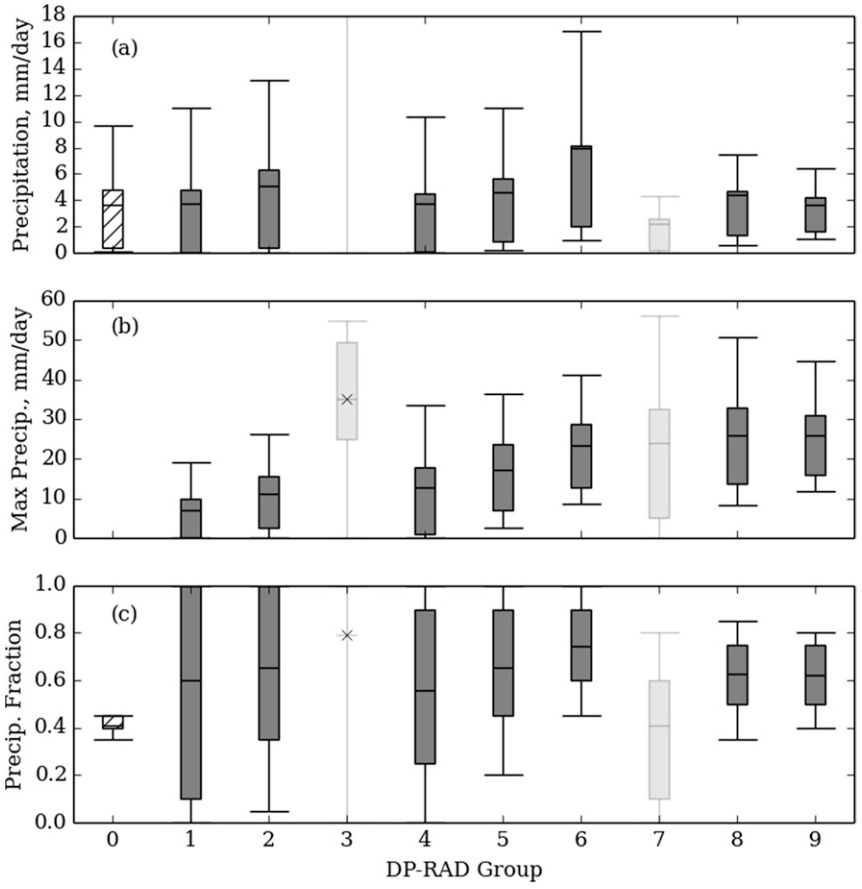

FIG. 13. Composite statistics of precipitation for all groups, including nonstormy group $\mathbb{G}0$: (a) daily, (b) maximum, and (c) fraction. Whiskers are the 10th- and 90th-percentile values of each metric. Box edges are the 25th- and 75th-percentile values. Mean values are denoted with a black line. Mean values for $\mathbb{G}3$ are marked with an $\times$, where sparseness prevents percentile calculation. Mean of $\mathbb{G}3$ average precipitation in (a) exceeds vertical scale at 32.18 mm day^{-1}.

radiation available. We consider the representation of each center in four ways: the average, maximum, minimum, or entire distribution of all available values within that center's area. The contribution of each center is then either a single value (in the case of the average, maximum, or minimum) or a distribution (of multiple values), which is then added to the composite distribution for the associated depth–radius group. When each center is represented by a single value, the dispersion of the resulting composite distributions for a given depth–radius group quantifies storm-to-storm differences between cyclones of that group.

We find little difference in the composite distributions between groups when each center is represented by the average of its collocated values. This result does not change when distributions are created using every measurement within the storm rather than the average; thus, we present the latter for simplicity. We find significant differences between groups when distributions are constructed using the extreme values, however. This emphasizes the importance of within-storm differences, which are a component of the intragroup (storm to storm) differences but are obscured by representing each cyclone center as an average of estimates.

In these statistical analyses we build distributions corresponding to the average, maximum, or minimum precipitation and CRE values associated with each cyclone. To characterize the storm-to-storm dispersion within a group, we use the difference between the 90th- and 10th-percentile values of each distribution to represent the variability for each group. In all cases, the least frequent groups $\mathbb{G}3$ and $\mathbb{G}7$ are lightly shaded to deemphasize their significance (Figs. 13 and 14) because of very low sample sizes.

A summary of our findings is presented in Table 1, showing the dependency of precipitation and CRE on cyclone depth and radius. Note that the relationships in Table 1 are not robust throughout depth–radius space.

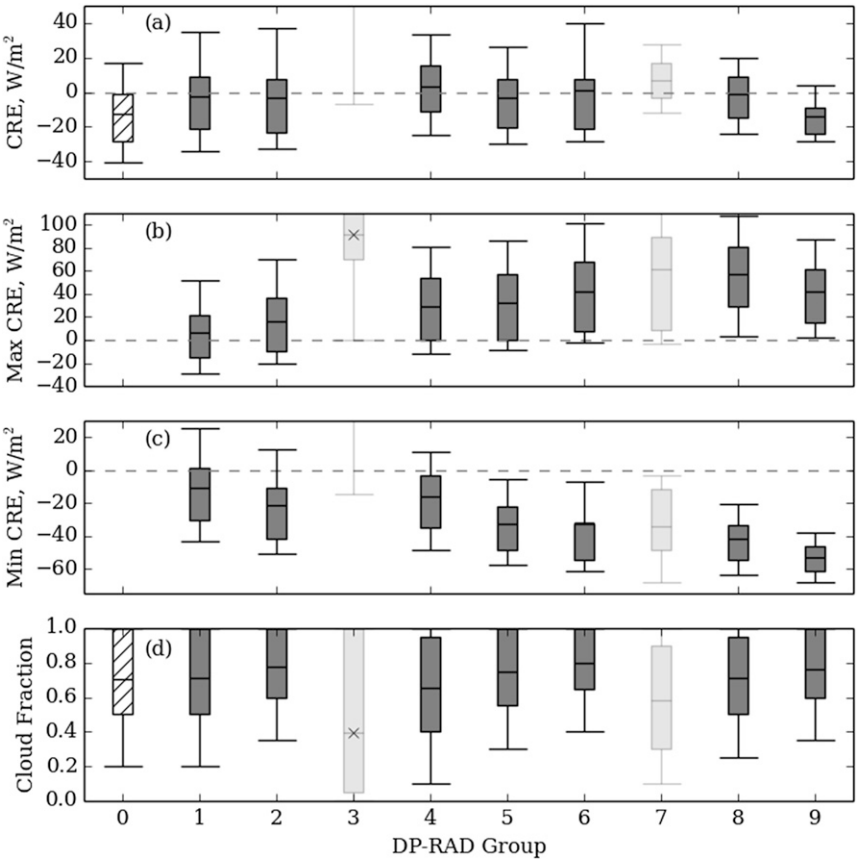

FIG. 14. As in Fig. 13, but for CRE: (a) mean of $\mathbb{G}3$ average, (b) mean of maximum, (c) mean of minimum, and (d) cloud fraction. Both (a) and (c) exceed vertical scale for $\mathbb{G}3$ at 90.02 and 88.41 W m^{-2}, respectively.

We discuss the details of precipitation and radiation with attention to the diagonal groups ($\mathbb{G}1$, $\mathbb{G}5$, and $\mathbb{G}9$): namely, small and shallow versus large and deep. Cyclones belonging to $\mathbb{G}5$ behave in an intermediate fashion in terms of both the magnitude and range of their composite distributions.

1) PRECIPITATION

Precipitation composites for all groups (using the storm area average) are shown in Fig. 13a. Aside from the most infrequent groups, the storm-average rates and distributions of precipitation are quite similar in all groups, including the nonstormy case. Because of the size differences between groups there are many more precipitation values associated with larger storms. Despite this, Fig. 13a shows that the composite distributions corresponding to the largest, deepest cyclones ($\mathbb{G}9$) are similar to those of smaller, shallower cyclones. The greatest mean area-average precipitation is found for $\mathbb{G}6$ at approximately 8 mm day^{-1}. Note that the average precipitation is negatively correlated with increasing size for groups of average depth ($\mathbb{G}2$, $\mathbb{G}5$, and $\mathbb{G}8$), suggesting more small values for larger storms and perhaps larger areas corresponding to the cold sector.

When composite distributions are assembled using the maximum precipitation from each storm's region of influence, differences between the groups begin to appear, as shown in Fig. 13b. Maximum precipitation increases for deeper and larger storms (e.g., $\mathbb{G}9$); however, this is accompanied by increased variability. Compared with smaller groups, these largest storms have greater differences between storms in the same group. As depth increases, however, the variability of the distributions corresponding to the largest groups decreases, which means decreasing differences between storms of the same group and more consistency among the deepest groups, indicating a coupled relationship between depth and precipitation.

Pfahl and Wernli (2012) find that cyclones responsible for precipitation extremes are not significantly more intense than others. Our result showing the correlation between depth and increased precipitation does not agree

TABLE 1. Summary of cyclone composite dependencies on increasing size and radius. Each property is labeled with either ↑ (increases for all groups) or ↓ (decreases for all groups). CRE composites for larger storms (⇓: decrease with depth) differ from smaller and average-size storms (⇑: increase with depth). Invariance to changes in either property are indicated (–) accordingly. The *R* and *D* stand for radius and depth, respectively.

	Value		Range	
Max precipitation	↑	↑	↑	↓
Precipitation fraction	—	↑	↓	↓
Max CRE	↑	⇑ ⇓	—	⇑ ⇓
Min CRE	↓	↓	↓	— ⇓
Cloud fraction	—	↑	↑	↓
	↑ *R*	↑ *D*	↑ *R*	↑ *D*

with their assertion. However, we do not limit our analysis to extreme events, and we collect precipitation estimates following each storm's path in a Lagrangian sense, whereas Pfahl and Wernli (2012) define extreme as the 99th percentile of precipitation at a given location. The correlation between precipitation and depth we observe is a general relationship across a broad range of depth and precipitation values, not focusing only on the rarest 1% of events. Furthermore, their intensity metric is central SLP, which we have shown to be a poor metric for a global intercomparison of cyclones and differs from ours. In a separate study by Pfahl and Sprenger (2016), the authors observe a relationship between precipitation and intensity; however, they also note that intensity alone does not imply greater rain rates: the presence of water vapor strongly influences precipitation.

Distributions of average precipitation within each storm (Fig. 13a) obscure differences between larger, deeper (e.g., $\mathbb{G}9$) and smaller, shallower (e.g., $\mathbb{G}1$) groups. Average precipitation associated with $\mathbb{G}1$, $\mathbb{G}2$, and $\mathbb{G}4$ has 10th-percentile values of $0\,\mathrm{mm\,day^{-1}}$, indicating that a few storms belonging to these groups have no precipitation within their region of influence. It is likely that these smaller, shallower storms are immature and generate precipitation in later stages of evolution (perhaps associated with another group). Furthermore, there may be precipitation associated with a remote front outside the stormy region. All other groups that have a small but nonzero 10th-percentile value have a mixture of precipitating and nonprecipitating regions. To quantify the statistical effects of nonprecipitating locations within the cyclone, we define a precipitation fraction (PF) for each cyclone as $\mathrm{PF} = \overline{P}_0/\overline{P}$, where $\overline{P}_0$ is the average precipitation within the cyclone including zero-valued estimates, and $\overline{P}$ is the average omitting zeros. The ratio takes on values between 0 and 1, where a larger ratio implies more precipitating locations within the storm.

PF distributions for all groups are shown in Fig. 13c. Smaller, shallower groups (e.g., $\mathbb{G}1$ and $\mathbb{G}4$) exhibit an increased variability in distributions of PF, indicating larger differences between storms in the same group. Within these smaller, shallower groups there exist cyclones that are either raining everywhere (PF = 1.0), nowhere (PF = 0.0), or at scattered locations within the region of influence. The opposite behavior is observed for deeper, larger groups (e.g., $\mathbb{G}9$), which show decreased variability of PF: thus, similar fractions of precipitating area among storms of the same group. Larger storms have an increase of zero precipitation values proportional to their additional area, which explains the contrast between composite distributions constructed using the average precipitation rather than the maximum. While raining more consistently than storms of smaller groups, the variability of maximum precipitation shows that, in terms of peak rain rate, large storms differ more strongly among one another than smaller storms. This emphasizes the need to more closely inspect the interior of these storms.

In terms of the cyclone-associated energy contribution to the atmosphere, the most intense precipitation rates will result in proportionally strong latent heating locally. The contribution of each depth–radius group to this heating depends on the rain rate integrated over the entire area of each storm and the group frequency of occurrence. While larger areas are not entirely filled with precipitating locations, larger storms contain more instances of precipitation and may produce more heating than a smaller storm with the same average precipitation. Similarly, interiors of smaller storms may precipitate more uniformly (PF = 1.0); however, a smaller precipitating fraction of a larger storm may result in a larger contribution to the overall latent heating. Considering the similar maximum precipitation rates for $\mathbb{G}6$ and $\mathbb{G}9$, the increased frequency of $\mathbb{G}9$ in combination with its size (viz. more total area-integrated precipitation) makes its total heating contribution much more significant.

Given the simple relationship between depth and precipitation, it is natural to consider the wind speed intensity metric $\hat{\mathbb{U}}$ in the context of precipitation. Intensity depends linearly on depth and is greatest for groups on the smaller, deeper side of the group 1–5–9 diagonal. We showed in section 4b that these intense groups also exhibit relatively increased frequency for winter seasons. In a study quantifying the cyclone component of NH precipitation, Hawcroft et al. (2012) find that the contribution to total cyclone precipitation from the most intensely precipitating 10% of all storms is greater in winter than in summer. They report that this top 10% of storms is responsible for 20% of the overall

cyclone precipitation in winter, but for only 15% of the total in summer. Their result supports the relationships we find between deeper, cool season cyclones with relatively greater precipitation.

It seems reasonable that the most intense storms are also those with the greatest turbulent kinetic energy, implying vigorous vertical motion, leading to intense precipitation, as we observe for $\mathbb{G}6$ and $\mathbb{G}9$. Pfahl and Sprenger (2016) find that precipitation prior to the storm's peak intensity is strongly correlated with cyclone intensity, lending support to this notion. At the same time, the larger storms ($\mathbb{G}9$) contain a significant proportion of nonprecipitating regions (smaller PF). Upward motion within the cyclone is accompanied by subsidence, which accounts for the nonprecipitating regions that exist throughout the largest, deepest cyclones. Further investigation of spatial distributions of precipitation in a similar style as Field and Wood (2007) will clarify the relationship between intensity and precipitation.

2) Radiation: In-atmosphere cloud radiative effect

The radiative influence of storm clouds is assessed through the SW and LW CRE flux divergence between SRF and TOA, giving the atmospheric net radiation. In general, area-average CRE is slightly negative for all cyclones (Fig. 14a), which implies an overall cooling effect on the atmosphere relative to clear sky. Information on the attribution of fluxes to clear sky and all sky is available in Zhang et al. (2004). Storm area-average CRE shows few robust relationships between size or depth. However, the largest groups show decreased variability and enhanced cooling with increasing depth. Area-averaged CRE associated with nonstormy areas does not differ significantly from stormy regions, including the most intense cyclones in $\mathbb{G}9$.

Intergroup differences are more apparent in composite distributions of CRE extremes, shown in Figs. 14b and 14c. Maximum CRE is generally positive for all groups, implying enhanced heating by clouds, and minimum CREs are mostly negative for all groups, corresponding to enhanced cooling. Distributions of minimum CRE shift to more negative values with both increasing size and depth; however, the change with depth is greater than that associated with radius. Because we calculate the net in-atmosphere CRE using SW and LW fluxes from TOA and SRF, heating and cooling do not imply vertical location of cloud.

The CRE values of greatest magnitude are associated with larger, deeper cyclones. In both the maximum and minimum cases, mean values of the group CRE distributions vary by approximately $50\,\mathrm{W\,m^{-2}}$ between the strongest and weakest (in the radiative sense) groups. Despite these intergroup differences in CRE, differences in average cloud fraction (CF; Fig. 14d) are small compared to the differences in CF variability that decrease for larger, deeper storms. Furthermore, average CF values for cyclone groups do not greatly differ from the $\mathbb{G}0$ case, which is consistent with the findings of Tselioudis et al. (2000). While there are not significant intergroup differences in CF, the seasonal variability of the groups themselves may contribute to the NH seasonal variability of cyclone cloud cover, as found in Naud et al. (2013). That said, Naud et al. (2013) focused on oceanic cyclones, whereas the depth–radius groups considered here combine cyclones over land and ocean, so it is not possible to directly compare the seasonal variability found in Naud et al. (2013) using only the seasonal variability of groups.

Compared with the smaller, shallower groups, there is similar storm-to-storm variation in maximum CRE heating among larger, deeper groups. In contrast, the minimum CRE cooling associated with larger, deeper storms exhibits much less storm-to-storm variation than smaller, shallower groups. This suggests more clear-sky conditions associated with larger storms and is consistent with the larger number of zero-value precipitation estimates associated with these larger storms. We comment that calculation of CRE depends on clear sky, the occurrence of which differs between hemisphere, season, and land–ocean surface type (Zhang et al. 2004). These variations in clear sky complicate attributing changes in CRE to changes in cyclone depth or radius only.

In summary, deeper and larger storms have more extreme CRE values, which are obscured in the average. These extrema take the form of heating and cooling, which require both turbulent vertical motions and suppressed conditions. While depth serves to homogenize the behavior of the largest storms, it acts to diversify the radiation character of smaller groups. The largest and deepest $\mathbb{G}9$ cyclones will have the most significant radiative impact on the atmosphere as a result of their greater frequency of occurrence and substantial size. Despite significant heating by clouds of these largest, deepest storms, the enhanced cooling effects offset the warming in the mean.

5. Conclusions

In this paper, we analyze over 10^6 cyclones identified in the ERAI by the MCMS tracking algorithm between 1979 and 2012. Our analysis includes properties of the cyclones themselves, as well as the composite precipitation and radiation values associated with each storm (from a shorter record). To investigate changes in the distribution of cyclone centers, we developed a "low

resolution'' joint histogram using cyclone radius and depth, though several alternative properties were considered. The nine groups defined by this joint distribution were compared with one another in terms of their intensity (wind speed proxy), seasonal and interannual variability, geographic preference, and contribution to atmospheric diabatic heating by precipitation and cloud-induced radiation perturbations.

We find a positive correlation between depth and radius as the majority of cyclone centers exist in three groups: small and shallow, median size and depth, and very large and very deep. The correlation we find is sensitive to our definitions of size and depth, and other studies with various other definitions of these properties have reported varying degrees of dependence between depth and radius (Simmonds 2000; Rudeva and Gulev 2007; Schneidereit et al. 2010). Because of the monomodal skewed distribution shapes of both radius and depth, the deepest and largest group $\mathbb{G}9$ has no upper bound in either dimension and has the greatest range of both properties among all groups.

Greatest intensities are found for cyclones belonging to the deepest groups, and we find that intensity depends strongly on the cyclone depth while exhibiting little size dependence. There are few differences between intensity distributions of groups that have similar depth but a large range of sizes. Though there exists a positive correlation between size and depth, size does not imply a more intense storm.

The groups defined by the joint distribution allow us to investigate seasonal variability in the distribution of cyclone centers. We find that NH variability is much stronger than in the SH and that there exists a seasonal pattern for both hemispheres in which smaller, deeper (more intense) centers are more frequent in cool seasons. Similarly, we observe that larger, shallower (less intense) centers are more frequent in warm seasons. Persistent throughout these seasonal shifts is the positive correlation between depth and radius. While maintaining the correlations, the distribution of cyclone centers shifts from one side of the diagonal to the other, alternating between warm and cool seasons.

Our analysis of seasonal variability shows that the meridional distributions of cyclone centers differ between the Northern and Southern Hemispheres, as shown in several previous studies (Hoskins and Hodges 2002, 2005; Wernli and Schwierz 2006). In the NH, a poleward shift of group frequency peaks is observed during warm seasons. This meridional shift in peak frequency is not observed for SH groups, suggesting that surface differences (land–ocean) between hemispheres may be one component responsible for the different seasonal modes of variability. SH seasonal variability is observed as either amplification or attenuation of fixed meridional distribution shapes with no poleward shift of the group frequency peak. This does not disagree with earlier work: for example, in the SH, Simmonds and Keay (2000a) showed the zone of greatest radii shifted poleward in summer, and the zone of greatest depth shifted poleward in winter. The depth–radius groups we defined have different corresponding meridional distributions. Rather than a seasonal shift observed within a single group (as in the NH) a SH poleward shift may manifest as changes in the frequencies of multiple groups whose superposition results in a net poleward shift of properties without a meridional shift of any particular group frequency.

Several studies suggest that a poleward shift of storm tracks may occur in a warming climate (Fyfe 2003; Carnell and Senior 1998; Bender et al. 2012; Hartmann et al. 2013; Wang et al. 2013). We have shown that the seasonal variability is distinctly different between hemispheres: NH cyclone frequency peaks shift meridionally between seasons, whereas SH cyclones become more or less frequent without a shift in the mode. While seasonal variability is not a proxy for a warming climate, it does show a hemispheric difference in the relationship between temperature and storm-track position. Thus, it is important to understand the physical reasons for this hemispheric asymmetry, and reproduce it in models, before making successful predictions of storm-track position in a warming climate.

Spatial distributions of various depth–radius cyclone groups reveal hemispheric differences and a consistent preference of certain groups for certain surface types. Shallow centers prefer land, where deep centers are more often found over ocean. While average depth centers exist over a mixture of surface types, there is a ''second order'' dependence between cyclone radius and surface type: smaller centers prefer land, while larger centers are more often found over ocean. It is possible that this correlation between oceanic surfaces with greater depth and radius is in part due to the presence of readily available moisture over the ocean. It is known that moisture impacts the development of cyclones, as shown by Booth et al. (2013). They found wind speed and precipitation to be positively correlated with moisture in a series of numerical experiments. The presence of moisture may amplify the diabatic effects from precipitation and CRE, providing a positive feedback on cyclone development. We plan to address this in future investigations.

Stationary features, such as orography or persistent regions of low pressure, are also associated with particular depth–radius groups. Larger, shallower centers are often found near and in the lees of mountainous regions in both hemispheres. Smaller, deeper centers are often

TABLE A1. Fractions of centers that exist either among other centers within a multicenter contour or occupy their own single-center contour. In the MCC case, the proportion of NCs that are either primary or secondary is reported, as well as the corresponding depth–radius group of each.

	D–R classification (frequency; % of center type subset)								
Center type subset (frequency)	$\mathbb{G}1$	$\mathbb{G}2$	$\mathbb{G}3$	$\mathbb{G}4$	$\mathbb{G}5$	$\mathbb{G}6$	$\mathbb{G}7$	$\mathbb{G}8$	$\mathbb{G}9$
Single center (46.20% of total)	36.01	9.50	0.09	4.71	30.30	6.51	0.14	2.66	10.08
Multicenter (53.80% of total)	30.83	13.31	0.02	1.94	20.36	2.96	0.02	4.59	25.96
Primary (35.71% of NCs)	0.15	0.09	0.00	0.65	13.31	2.43	0.02	12.31	71.04
Secondary (64.29% of NCs)	47.87	20.66	0.03	2.66	24.28	3.26	0.02	0.30	0.92

found in regions of persistent low pressure. The major Atlantic and Pacific storm tracks are also apparent in our results, within which smaller, shallower centers appear further upstream, while larger, deeper centers are found further downstream. Similar findings have been reported by Hoskins and Hodges (2002), in which peak cyclone intensities are found on the downstream end of the two primary NH storm tracks. We plan to further investigate this observation in a separate lifetime study but comment that this arrangement indicates some evolution between depth–radius groups throughout lifetime.

The contribution to atmospheric heating from cyclone-associated precipitation and CRE is assessed through a composite study using the stormy region surrounding each cyclone center. In the average precipitation composites, the number of zero or very small values offsets the extreme values, resulting in little intergroup differences. The maximum precipitation rate is positively correlated with depth, and the variability of maximum precipitation decreases with depth: thus, there is more consistency between deeper storms.

Composites of cyclone area-average CRE exhibit a net cooling effect for all groups, which is enhanced somewhat with increasing depth. Distributions of maximum (minimum) CRE shift toward enhanced heating (cooling) for deeper storms. These large values are obscured in the average, which suppresses differences between the groups. With increasing depth and radius, there are more storm-to-storm differences within groups for (maximum) CRE heating than (minimum) cooling, suggesting that there is a lower limit on CRE cooling.

Variations of both precipitation and CRE within a storm are respectively represented by calculating PF and CF for each cyclone. We find that more intense groups (smaller and deeper) have more consistent proportions of regions filled with cloud or precipitation than less intense groups (larger and shallower). While these metrics provide a rough evaluation of the intrastorm variation, a detailed assessment of the cyclone interior (as in Field and Wood 2007; Naud et al. 2010, 2015) will help determine the nature of precipitation, CRE, and clouds in specific sectors of the cyclone.

Using the outermost closed SLP contour to delineate the compositing region captures much of the warm sector precipitation and clouds (Catto and Pfahl 2013). It is likely that more cold sector information is included for the larger cyclones—namely, cold frontal clouds and precipitation—which may skew the composited values of CRE and precipitation. The fact that we observe a correlation between depth and radius means that composites of the deepest cyclones are also more likely to include some cold sector information, which may have been excluded in smaller, shallower storms. In comparing storms of different sizes, it would be ideal to include equal proportions of cold and warm sectors. The cold sector is where Bodas-Salcedo et al. (2012) reported the greatest bias in SW cloud forcing, which emphasizes the importance of studying these regions.

Results presented here indicate that the deepest cyclones are responsible for extreme values of precipitation and radiation, and, as a result of area and frequency, the deepest and largest are associated with the greatest diabatic heating. This analysis of cyclone center properties, variability, and their associated energetics provides a foundation for the continued study of cyclone lifetime and the spatial distribution of heating due to precipitation and radiation within the cyclone interior.

Acknowledgments. The authors wish to thank the three anonymous reviewers for their insightful comments and suggestions. J. P. wishes to thank Michael Bauer for many helpful discussions and to acknowledge Python's matplotlib package (Hunter 2007), Jeffrey Whitaker for the development of the Basemap toolkit for matplotlib, and the support of NOAA/EPP (Grant NA11SEC4810004). W. R. wishes to acknowledge the support of the NSF (Award 1240643).

APPENDIX

Entanglement

More than half of all identified centers are entangled (see Fig. 1). It is important to discuss the nature of these

TABLE A2. Secondary center frequencies for each depth–radius group and center type (attributed or empty). Also reported (bottom row) is the frequency of secondary centers that are associated with a primary center of the corresponding group (e.g., 24.28% of all secondary centers belong to $\mathbb{G}5$, but only 8.30% of all secondary centers are associated with a $\mathbb{G}5$ primary center).

	D–R classification (frequency; % of subset)								
Secondary center type (frequency; %)	$\mathbb{G}1$	$\mathbb{G}2$	$\mathbb{G}3$	$\mathbb{G}4$	$\mathbb{G}5$	$\mathbb{G}6$	$\mathbb{G}7$	$\mathbb{G}8$	$\mathbb{G}9$
ANC (63.10)	37.55	24.05	0.05	2.31	30.47	4.60	0.01	0.24	0.74
ENC (36.90)	65.52	14.86	0.00	3.27	13.71	0.98	0.02	0.42	1.23
NC (100.00)	47.87	20.66	0.03	2.66	24.28	3.26	0.02	0.30	0.92
Secondary–primary association	0.08	0.05	0.00	0.37	8.30	1.48	0.01	11.47	78.23

centers for three reasons. First, the decision to collapse secondary onto primary centers affects all NCs and needs justification. Second, it is a useful demonstration of the value of the depth–radius classification scheme (the discussion here makes use of the $\mathbb{G}X$ notation described in the main text and group thresholds corresponding to the precollapse case). Third, entangled cases are a frequently occurring complex interaction between low-pressure features—which may be merging or bifurcating—and is deserving of further study beyond what is presented herein.

Cyclone centers are roughly equally split between single-center contours (SCCs) or MCCs and the frequencies for each depth–radius group are reported in Table A1 with the corresponding proportion of primary or secondary NCs in the MCC case. No NCs exist within an SCC. Table A1 shows the majority of SCC centers are smaller, shallower disturbances, whereas a larger proportion of MCC centers belong to the largest, deepest group.

Approximately one-third of MCC centers are primary centers (the others collectively referred to as secondary centers), meaning they have the lowest SLP of all centers in the same MCC. Nearly all (83%) of these primary MCC centers are in the largest three groups. The remaining centers within an MCC are secondary centers, 91% of which are of median size or smaller and of median depth or shallower (Table A2). We computed the difference of depth and radius between primary centers and their associated secondary centers in the same MCCs and found that both the depth and radius are (nearly) always much greater for primary centers (not shown, and not due to the definition of a primary center either). The few exceptions to this occur where a large or deep secondary center is associated with a small or shallow primary center with a lower absolute center pressure, but a shallower depth as a result of the shape of the SLP surface (a lower center pressure does not imply greater depth).

While the secondary centers themselves often belong to smaller, shallower groups, they are in the same MCC as a primary center that belongs to a larger, deeper group (Table A2, bottom row). Approximately two-thirds of all secondary centers themselves belong to the smallest groups $\mathbb{G}1$ and $\mathbb{G}2$, and nearly 90% of all secondary centers are associated with a $\mathbb{G}8$ or $\mathbb{G}9$ primary center.

These observations show that secondary centers are generally smaller pressure perturbations in the vicinity of a deeper, larger-scale disturbance. This motivated our decision to collapse secondary centers onto their respective primary center. This involves adding individual area contributions of each collapsed center, along with the stormy area within the MCC, to the area of the associated primary center. Each primary center is also assigned the depth of the corresponding stormy region (see section 3 for details), which is always greater than the depths of the contained centers (not shown). Collapsing the secondary centers in this way shifts the distribution of primary centers toward greater depths and radii, and thus the depth–radius group definition thresholds are shifted to greater values. Aside from this change, the joint distribution shape and group frequencies are nearly identical before and after collapse; thus, secondary centers are not responsible for the distribution shape.

REFERENCES

Allan, R. P., and B. J. Soden, 2007: Large discrepancy between observed and simulated precipitation trends in the ascending and descending branches of the tropical circulation. *Geophys. Res. Lett.*, **34**, L18705, doi:10.1029/2007GL031460.

Bauer, M., G. Tselioudis, and W. B. Rossow, 2016: A new climatology for investigating storm influences in and on the extratropics. *J. Climate*, **55**, 1287–1303, doi:10.1175/JAMC-D-15-0245.1.

Bender, F. A. M., V. Ramanathan, and G. Tselioudis, 2012: Changes in extratropical storm track cloudiness 1983–2008: Observational support for a poleward shift. *Climate Dyn.*, **38**, 2037–2053, doi:10.1007/s00382-011-1065-6.

Benestad, R. E., and D. Chen, 2006: The use of a calculus-based cyclone identification method for generating storm statistics. *Tellus*, **58A**, 473–486, doi:10.1111/j.1600-0870.2006.00191.x.

Bodas-Salcedo, A., K. D. Williams, P. R. Field, and A. P. Lock, 2012: The surface downwelling solar radiation surplus over the Southern Ocean in the Met Office model: The role of midlatitude cyclone clouds. *J. Climate*, **25**, 7467–7486, doi:10.1175/JCLI-D-11-00702.1.

Bony, S., and Coauthors, 2006: How well do we understand and evaluate climate change feedback processes? *J. Climate*, **19**, 3445–3482, doi:10.1175/JCLI3819.1.

Booth, J. F., S. Wang, and L. Polvani, 2013: Midlatitude storms in a moister world: Lessons from idealized baroclinic life cycle experiments. *Climate Dyn.*, **41**, 787–802, doi:10.1007/s00382-012-1472-3.

Carnell, R. E., and C. A. Senior, 1998: Changes in mid-latitude variability due to increasing greenhouse gases and sulphate aerosols. *Climate Dyn.*, **14**, 369–383, doi:10.1007/s003820050229.

Catto, J. L., and S. Pfahl, 2013: The importance of fronts for extreme precipitation. *J. Geophys. Res. Atmos.*, **118**, 10 791–10 801, doi:10.1002/jgrd.50852.

——, L. C. Shaffrey, and K. I. Hodges, 2010: Can climate models capture the structure of extratropical cyclones? *J. Climate*, **23**, 1621–1635, doi:10.1175/2009JCLI3318.1.

Dee, D. P., and Coauthors, 2011: The ERA-Interim reanalysis: Configuration and performance of the data assimilation system. *Quart. J. Roy. Meteor. Soc.*, **137**, 553–597, doi:10.1002/qj.828.

Field, P. R., and R. Wood, 2007: Precipitation and cloud structure in midlatitude cyclones. *J. Climate*, **20**, 233–254, doi:10.1175/JCLI3998.1.

Fyfe, J. C., 2003: Extratropical Southern Hemisphere cyclones: Harbingers of climate change? *J. Climate*, **16**, 2802–2805, doi:10.1175/1520-0442(2003)016<2802:ESHCHO>2.0.CO;2.

Govekar, P. D., C. Jakob, and J. Catto, 2014: The relationship between clouds and dynamics in Southern Hemisphere extratropical cyclones in the real world and a climate model. *J. Geophys. Res. Atmos.*, **19**, 6609–6628, doi:10.1002/2013JD020699.

Grotjahn, R., D. Hodyss, and C. Castello, 1999: Do frontal cyclones change size? Observed widths of North Pacific lows. *Mon. Wea. Rev.*, **127**, 1089–1095, doi:10.1175/1520-0493(1999)127<1089:DFCCSO>2.0.CO;2.

Hartmann, D. L., and Coauthors, 2013: Observations: Atmosphere and surface. *Climate Change 2013: The Physical Science Basis*, T. F. Stocker et al., Eds., Cambridge University Press, 159–254, doi:10.1017/CBO9781107415324.008.

Hawcroft, M. K., L. C. Shaffrey, K. I. Hodges, and H. F. Dacre, 2012: How much Northern Hemisphere precipitation is associated with extratropical cyclones? *Geophys. Res. Lett.*, **39**, L24809, doi:10.1029/2012GL053866.

Haynes, J. M., C. Jakob, W. B. Rossow, G. Tselioudis, and J. Brown, 2011: Major characteristics of Southern Ocean cloud regimes and their effects on the energy budget. *J. Climate*, **24**, 5061–5080, doi:10.1175/2011JCLI4052.1.

Hodges, K. I., R. W. Lee, and L. Bengtsson, 2011: A comparison of extratropical cyclones in recent reanalyses ERA-Interim, NASA MERRA, NCEP CFSR, and JRA-25. *J. Climate*, **24**, 4888–4906, doi:10.1175/2011JCLI4097.1.

Hoskins, B. J., and K. I. Hodges, 2002: New perspectives on the Northern Hemisphere winter storm tracks. *J. Atmos. Sci.*, **59**, 1041–1061, doi:10.1175/1520-0469(2002)059<1041:NPOTNH>2.0.CO;2.

——, and ——, 2005: A new perspective on Southern Hemisphere storm tracks. *J. Climate*, **18**, 4108–4129, doi:10.1175/JCLI3570.1.

Houze, R. A., and P. V. Hobbs, 1982: Organization and structure of precipitating cloud systems. *Advances in Geophysics*, Vol. 24, Academic Press, 225–315, doi:10.1016/S0065-2687(08)60521-X.

Huffman, G. J., R. F. Adler, M. M. Morrissey, D. T. Bolvin, S. Curtis, R. Joyce, B. McGavock, and J. Susskind, 2001: Global precipitation at one-degree daily resolution from multisatellite observations. *J. Hydrometeor.*, **2**, 36–50, doi:10.1175/1525-7541(2001)002<0036:GPAODD>2.0.CO;2.

Hunter, J. D., 2007: Matplotlib: A 2D graphics environment. *Comput. Sci. Eng.*, **9**, 90–95, doi:10.1109/MCSE.2007.55.

Kanamitsu, M., W. Ebisuzaki, J. Woollen, S.-K. Yang, J. J. Hnilo, M. Fiorino, and G. L. Potter, 2002: NCEP–DOE AMIP-II reanalysis (R-2). *Bull. Amer. Meteor. Soc.*, **83**, 1631–1643, doi:10.1175/BAMS-83-11-1631.

Lau, N.-C., and M. W. Crane, 1995: A satellite view of the synoptic-scale organization of cloud properties in midlatitude and tropical circulation systems. *Mon. Wea. Rev.*, **123**, 1984–2006, doi:10.1175/1520-0493(1995)123<1984:ASVOTS>2.0.CO;2.

Mason, S., J. K. Fletcher, J. M. Haynes, C. Franklin, A. Protat, and C. Jakob, 2015: A hybrid cloud regime methodology used to evaluate Southern Ocean cloud and shortwave radiation errors in access. *J. Climate*, **28**, 6001–6018, doi:10.1175/JCLI-D-14-00846.1.

Naud, C. M., A. D. Del Genio, M. Bauer, and W. Kovari, 2010: Cloud vertical distribution across warm and cold fronts in *CloudSat–CALIPSO* data and a general circulation model. *J. Climate*, **23**, 3397–3415, doi:10.1175/2010JCLI3282.1.

——, D. J. Posselt, and S. C. van Den Heever, 2012: Observational analysis of cloud and precipitation in midlatitude cyclones: Northern versus Southern Hemisphere warm fronts. *J. Climate*, **25**, 5135–5151, doi:10.1175/JCLI-D-11-00569.1.

——, J. F. Booth, D. J. Posselt, and S. C. van den Heever, 2013: Multiple satellite observations of cloud cover in extratropical cyclones. *J. Geophys. Res. Atmos.*, **118**, 9982–9996, doi:10.1002/jgrd.50718.

——, D. J. Posselt, and S. C. van den Heever, 2015: A *CloudSat–CALIPSO* view of cloud and precipitation properties across cold fronts over the global oceans. *J. Climate*, **28**, 6743–6762, doi:10.1175/JCLI-D-15-0052.1.

Neu, U., and Coauthors, 2013: IMILAST: A community effort to intercompare extratropical cyclone detection and tracking algorithms. *Bull. Amer. Meteor. Soc.*, **94**, 529–547, doi:10.1175/BAMS-D-11-00154.1.

Peixoto, J. P., and A. H. Oort, 1992: *Physics of Climate*. American Institute of Physics, 520 pp.

Pfahl, S., and H. Wernli, 2012: Quantifying the relevance of cyclones for precipitation extremes. *J. Climate*, **25**, 6770–6780, doi:10.1175/JCLI-D-11-00705.1.

——, and M. Sprenger, 2016: On the relationship between extratropical cyclone precipitation and intensity. *Geophys. Res. Lett.*, **43**, 1752–1758, doi:10.1002/2016GL068018.

Rudeva, I., and S. K. Gulev, 2007: Climatology of cyclone size characteristics and their changes during the cyclone life cycle. *Mon. Wea. Rev.*, **135**, 2568–2587, doi:10.1175/MWR3420.1.

Schneidereit, A., R. Blender, and K. Fraedrich, 2010: A radius–depth model for midlatitude cyclones in reanalysis data and simulations. *Quart. J. Roy. Meteor. Soc.*, **136**, 50–60, doi:10.1002/qj.523.

Simmonds, I., 2000: Size changes over the life of sea level cyclones in the NCEP reanalysis. *Mon. Wea. Rev.*, **128**, 4118–4125, doi:10.1175/1520-0493(2000)129<4118:SCOTLO>2.0.CO;2.

——, and K. Keay, 2000a: Mean Southern Hemisphere extratropical cyclone behavior in the 40-year NCEP–NCAR reanalysis. *J. Climate*, **13**, 873–885, doi:10.1175/1520-0442(2000)013<0873:MSHECB>2.0.CO;2.

——, and ——, 2000b: Variability of Southern Hemisphere extratropical cyclone behavior, 1958–97. *J. Climate*, **13**, 550–561, doi:10.1175/1520-0442(2000)013<0550:VOSHEC>2.0.CO;2.

Sinclair, M. R., and M. J. Revell, 2000: Classification and composite diagnosis of extratropical cyclogenesis events in the southwest Pacific. *Mon. Wea. Rev.*, **128**, 1089–1105, doi:10.1175/1520-0493(2000)128<1089:CACDOE>2.0.CO;2.

Tilinina, N., S. K. Gulev, I. Rudeva, and P. Koltermann, 2013: Comparing cyclone life cycle characteristics and their interannual variability in different reanalyses. *J. Climate*, **26**, 6419–6438, doi:10.1175/JCLI-D-12-00777.1.

Tselioudis, G., and W. B. Rossow, 2006: Climate feedback implied by observed radiation and precipitation changes with midlatitude storm strength and frequency. *Geophys. Res. Lett.*, **33**, L02704, doi:10.1029/2005GL024513.

——, Y. Zhang, and W. B. Rossow, 2000: Cloud and radiation variations associated with northern midlatitude low and high sea level pressure regimes. *J. Climate*, **13**, 312–327, doi:10.1175/1520-0442(2000)013<0312:CARVAW>2.0.CO;2.

Wang, X. L., V. R. Swail, and F. W. Zwiers, 2006: Climatology and changes of extratropical cyclone activity: Comparison of ERA-40 with NCEP–NCAR reanalysis for 1958–2001. *J. Climate*, **19**, 3145–3166, doi:10.1175/JCLI3781.1.

——, Y. Feng, G. P. Compo, V. R. Swail, F. W. Zwiers, R. J. Allan, and P. D. Sardeshmukh, 2013: Trends and low frequency variability of extra-tropical cyclone activity in the ensemble of twentieth century reanalysis. *Climate Dyn.*, **40**, 2775–2800, doi:10.1007/s00382-012-1450-9.

Wernli, H., and C. Schwierz, 2006: Surface cyclones in the ERA-40 dataset (1958–2001). Part I: Novel identification method and global climatology. *J. Atmos. Sci.*, **63**, 2486–2507, doi:10.1175/JAS3766.1.

Wielicki, B. A., and Coauthors, 2002: Evidence for large decadal variability in the tropical mean radiative energy budget. *Science*, **295**, 841–844, doi:10.1126/science.1065837.

Zhang, Y., W. B. Rossow, A. A. Lacis, V. Oinas, and M. I. Mishchenko, 2004: Calculation of radiative fluxes from the surface to top of atmosphere based on ISCCP and other global data sets: Refinements of the radiative transfer model and the input data. *J. Geophys. Res.*, **109**, D19105, doi:10.1029/2003JD004457.